

# Stability Comparison Between Grid-forming and Grid-following Based Wind Farms Integrated MMC-HVDC

Rongcai Pan, Dong Liu, Shan Liu, Jie Yang, Longze Kou, and Guangfu Tang

**Abstract**—Grid-forming (GFM) control based high-voltage DC (HVDC) systems and renewable energy sources (RESs) provide support for enhancing the stability of power systems. However, the interaction and coordination of frequency support between the GFM-based modular multilevel converter based HVDC (MMC-HVDC) and grid-following (GFL) based RESs or GFM-based RESs have not been fully investigated, which are examined in this study. First, the detailed AC- and DC-side impedances of GFM-based MMC-HVDC are analyzed. The impedance characteristics of GFL- and GFM-based wind turbines are next analyzed. Then, the influences of GFL- and GFM-based wind farms (WFs) on the DC- and AC-side stabilities of WF-integrated MMC-HVDC systems are compared and evaluated. The results show that the GFM-based wind turbine performs better than the GFL-based wind turbine. Accordingly, to support a receiving-end AC system, the corresponding frequency supporting strategies are proposed based on the GFM control for WF-integrated MMC-HVDC systems. The GFM-based WF outperforms the GFL-based WF in terms of stability and response time. Simulations in PSCAD/EMTDC demonstrate the DC- and AC-side stability issues and seamless grid support from the RESs, i.e., WFs, to the receiving-end AC system.

**Index Terms**—Renewable energy source (RES), modular multilevel converter (MMC), wind farm, grid-forming (GFM), high-voltage direct current.

## I. INTRODUCTION

THE penetration of power electronics based renewable energy sources (RESs) into power systems is rapidly increasing. Simultaneously, the voltage source converter based high-voltage direct current (VSC-HVDC) transmission tech-

nology, particularly the modular multilevel converter based HVDC (MMC-HVDC) [1], is being used in an increasing number of applications for the integration of large-scale centralized RESs such as BorWin2 and Dolwin3 projects for wind farm (WF) integration in Europe and the Zhangbei DC grid in China. Grid-following (GFL) control, which is widely used for RESs and VSC-HVDCs, is prone to instability caused by phase-locked loops (PLLs) in weak grids with high penetration of RESs [2]. In addition, power systems with high penetration of RESs may lack inertia and damping to suppress the high rate of change of frequency [2], [3]. Some accidents associated with decrease in inertia are reported, such as the event of August 9, 2019 in England [4].

To provide support for the power system without PLL [2], various GFM control methods for RESs and VSC-HVDCs have been proposed, including droop control, power synchronization control (PSC) [5], virtual synchronous machines/virtual synchronous generators (VSMs/VSGs) [3], [6], matching control [7], [8], and virtual oscillation control [9]. These methods are fully evaluated and discussed in [2]-[7]. In [6], the dynamic power decoupling for VSMs is analyzed to enhance the stability. A reference feedforward PSC is proposed in [10] for pole-zero cancellation to eliminate the step-response ringing and overshoot of the PSC. In [11] and [12], the low-frequency oscillations of a VSM-controlled VSC-HVDC are analyzed using the complex torque method and  $dq$  impedance method. The phase feedforward method [13] and virtual impedance [5], [10], [14] are proposed to damp the oscillation of the PSC and VSM, respectively. A unified VSM tuned with the transfer function method is proposed to coordinate a multi-terminal DC grid in [15]. In [16], the  $\mu$ -analysis is performed to investigate how the robust stability of a VSM converter is affected by another converter operating in parallel. However, these methods usually adopt an ideal DC voltage without considering RESs when analyzing GFM control.

Considering the GFM-based RESs, the photovoltaic VSG control and adaptive VSG control are proposed for photovoltaic systems with additional supercapacitors and battery energy storage [17], [18], and different modes are also proposed in [17] to satisfy different situations. In [19], the GFM control under different solar conditions with power reserves are devised for photovoltaic systems when considering DC-DC converters. The GFM control with short-term energy storage is proposed in [20] for Type-IV wind turbines, and a GFM-

Manuscript received: March 21, 2022; revised: July 5, 2022; accepted: September 20, 2022. Date of CrossCheck: September 20, 2022. Date of online publication: November 23, 2022.

This article is distributed under the terms of the Creative Commons Attribution 4.0 International License (<http://creativecommons.org/licenses/by/4.0/>).

This work was supported by National Key R&D Program of China (No. 2020YFB1506600).

R. Pan (corresponding author) is with China Electric Power Research Institute, Beijing 100192, China, and he is also with the State Key Laboratory of Advanced Power Transmission Technology and Beijing Key Laboratory of DC Grid Technology & Simulation, Beijing 102209, China (e-mail: prongc@yeah.net).

D. Liu, S. Liu, J. Yang, L. Kou, and G. Tang are with the State Key Laboratory of Advanced Power Transmission Technology and Beijing Key Laboratory of DC Grid Technology & Simulation, Beijing 102209, China (e-mail: liudong@geiri.sgcc.com.cn; liushan@geiri.sgcc.com.cn; yangjie@geiri.sgcc.com.cn; koulongze@geiri.sgcc.com.cn; gftang@geiri.sgcc.com.cn).

DOI: 10.35833/MPCE.2022.000158



based battery energy storage system is proposed for WFs in [21]. However, these studies focus only on RESs directly connected to AC systems. Whether these methods are suitable for RESs connected to MMC-HVDCs is not effectively determined.

These previous studies mostly focus on stability improvement of GFM-based VSC-HVDCs or GFM controller design for RESs, and thus pay less attention to GFM control interaction and coordination for frequency support between RESs and MMC-HVDCs. In addition, an engineering requirement exists for GFM-based MMC-HVDCs; for example, a WF-integrated MMC-HVDC of the Borwin6 project is required to adopt GFM control. Therefore, the stability interaction evaluation and coordination between the GFL-/GFM-based WFs and GFM-based MMC-HVDCs are vital to guarantee stable frequency support.

As shown Table I, in the effects of GFL-based WFs on MMC-HVDCs are studied in [26] and [27], and it is found that a GFL-based WF may cause instability between the WF and MMC. Neglecting the multi-harmonic frequency characteristics of MMC, the effects of GFM-based WFs on MMC-

HVDCs are discussed in [28]. In these studies, the MMC-HVDC adopts conventional control method, i. e., applying the DC voltage and voltage-frequency (VF) control for the receiving and sending ends, respectively, which cannot provide frequency support to the AC grid. When the frequency support to the receiving end by the MMC-HVDC is considered, many of the proposed coordination methods are enhanced based on conventional GFL control [22]-[25]. Only a few studies have considered GFM control for MMC-HVDCs to achieve frequency support, including the coordination strategy proposed in [29] for WF-integrated MMC-HVDCs. The MMC-HVDC adopts the GFM control while the WF adopts GFL control for grid supporting with PLLs. In addition, these studies also overlook the multi-harmonic characteristics of MMCs and GFL-based WFs, which may malfunction in weak grids with a slow frequency response. Considering the multi-harmonic characteristic and coordination control for frequency support, a systematic study of the effects of GFM- and GFL-based WF integration on GFM-based MMC-HVDCs is required, as summarized in Table I.

TABLE I  
COMPARISON OF METHODS IN DIFFERENT REFERENCES

Reference	Advantage	Disadvantage
[5], [6], [10], [13-16]	Performance analysis and enhancement of GFM	Ideal DC voltage without considering RESs
[17]-[21]	Grid support from RESs	Grid support feasibility after integration with MMC-HVDC
[22]-[25]	Grid support with RESs and MMC-HVDC	Conventional GFL control for MMC-HVDC and RESs
[26], [27]	MMC-HVDC connected to RESs with multi-harmonic dynamic	Conventional MMC-HVDC and RESs without grid support
[28], [29]	Grid support with GFM-based RESs or MMC-HVDC	Conventional GFL control for RESs or MMC-HVDC with neglecting multi-harmonic dynamic of MMC
Proposed	Grid support stability evaluation of GFM- and GFL-based RESs and MMC-HVDC with multi-harmonic dynamic and coordination strategy	RES dynamic is partially neglected and feasibility for large transient stability is not discussed

This study focuses on the GFM-based MMC-HVDC in a weak grid. Accordingly, the effects of the GFM- and GFL-based WFs on the GFM-based MMC-HVDC are evaluated using impedance modeling. Following a stability analysis, the GFM-based coordination control methods for WF-integrated MMC-HVDC systems are proposed to optimize the grid support function of the WF to support the receiving-end AC system. WFs and MMC-HVDCs both adopt GFM control in the proposed coordination control, which differs from the method proposed in [29]. The main contributions of this paper are as follows.

1) The impedance modeling of GFM-based MMC-HVDC is presented in a unified model using the harmonic transfer function [27]. The detailed impedance modeling for wind turbines with GFM and GFL control is presented. It is found that the coupling terms are non-negligible for AC-side stability.

2) The effects of GFM- and GFL-based WFs on the DC- and AC-side stabilities are compared, and this study determines that the effects of the inner parameters of the WF under different control modes have opposite effects on the DC-side stability. Although DC dynamics have practically no influence on the AC-side stability in a weak grid, the GFM-

based WF is preferable and can be used to enhance WF stability.

3) Accordingly, the revised coordination strategies are proposed for frequency support. In addition, a comparison with a traditional GFL-based WF with ancillary frequency support control is presented, while the proposed method outperforms a GFL-based WF, exhibiting a faster response and better stability.

As explained later in this paper, the machine-side dynamics of the WF are neglected, and therefore, the large transient stability is not discussed. The remainder of this paper is organized as follows. Section II establishes the impedance modeling of GFM-based MMC-HVDCs. Then, the impedance modeling of WFs with GFM and GFL controls are presented in Section III. The impedance verifications are described in Section IV for both MMCs and WFs. Case studies and the corresponding coordination strategies are given in Section V, and Section VI concludes this paper.

## II. IMPEDANCE MODELING OF GFM-BASED MMC-HVDCS

Figure 1 shows the diagram of a typical WF-integrated MMC-HVDC system. Each phase of the MMC consists of

upper and lower arms, which are composed of  $N$  submodules (SMs) as well as arm inductor  $L_{arm}$  and resistance  $R_{arm}$ . Each SM has a half-bridge structure with a capacitor  $C_m$ . The sum of each SM capacitor voltage for each arm is denoted as  $u_{xk}^\Sigma$ ,  $x=a,b,c$  denotes the three phase, and  $k=u,l$  denotes the upper and lower arms, respectively;  $u_{xk}$ ,  $m_{xk}$ ,  $i_{xk}$ ,  $i_{gx}$  and  $u_{sx}$  are the equivalent arm voltage, arm modulation index, arm current, grid current, and point of common connection (PCC) voltage, respectively;  $u_{dc}$  is the DC voltage; and  $v_o$  is the voltage from the DC midpoint to the neutral point. The offshore WF-side MMC (WFMMC) and onshore grid-side MMC (GSMMC) are connected to the WF sending-end AC grid and receiving-end AC grid with offshore and onshore AC transmission line  $L_{off}$  and  $L_{on}$ , respectively. The DC outlets of the GSMMC and WFMMC are generally connected through DC cable  $Z_{dc}$ , which is not considered in this study, i.e.,  $Z_{dc}=0$ , because our main focus is the effects of WF on the AC- and DC-side stabilities of the WF-integrated

MMC-HVDC system. Here, Type-IV WF is an aggregation of homogeneous wind turbines with current and voltage as  $i_s^{wt}$  and  $u_s^{wt}$ , respectively, as shown in Fig. 1. The number of wind turbines is denoted as  $N_{wt}$ , where the controlled current source is used to accurately represent the output impedance characteristics. This assumption for WF is valid in many small-signal stability studies, where the influence of the machine side is not significant and can thus be neglected, and the DC voltage is assumed to be constant with the allowable power output [26], [27], [30]. The sending-end AC grid is connected to the WFMMC via a step-up transformer whose ratio is  $K_t$ . Here, the leakage of the transformer is termed into the offshore AC line as part of  $L_{off}$ . The DC voltage of the wind turbine is denoted as  $u_{dc}^{wt}$ . The variables of the wind turbine are given by the superscript "wt" to distinguish them from those of the MMC, but in the following, the superscript is often omitted for simplification and to avoid confusion.

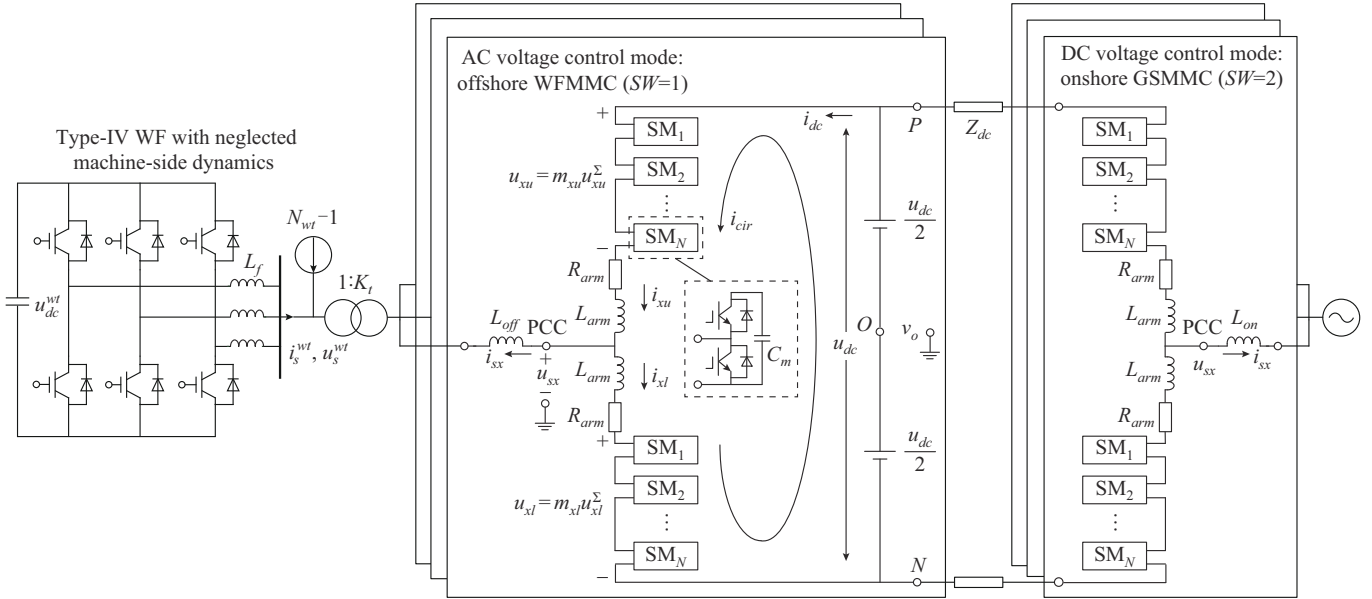


Fig. 1. Diagram of typical WF-integrated MMC-HVDC system.

### A. Power Stage of MMC

According to the averaged model of the MMC and Kirchhoff's law, the power stage equation can be derived as:

$$\begin{cases}
 L_{arm} \frac{di_{xu}}{dt} + R_{arm} i_{xu} = \frac{u_{dc}}{2} - u_{xu} - u_{sx} + v_o \\
 L_{arm} \frac{di_{xl}}{dt} + R_{arm} i_{xl} = \frac{u_{dc}}{2} - u_{xl} + u_{sx} - v_o \\
 u_{xu} = m_{xu} u_{xu}^\Sigma \\
 u_{xl} = m_{xl} u_{xl}^\Sigma \\
 \frac{C_m}{N} \frac{du_{xu}^\Sigma}{dt} = m_{xu} i_{xu} \\
 \frac{C_m}{N} \frac{du_{xl}^\Sigma}{dt} = m_{xl} i_{xl}
 \end{cases} \quad (1)$$

In fact, the third-order harmonic  $(\pm 3f_1, \pm 2f_1, \pm f_1, 0)$  modeling is sufficient to capture the steady-state characteristics of MMC accurately. When the perturbation voltage or cur-

rent is injected at the DC side or AC side, the main perturbation response also contains frequencies of less than third-order harmonics  $(f_p \pm 3f_1, f_p \pm 2f_1, f_p \pm f_1, f_p)$ . Note that the notations with phase are omitted because of the sequence relation given in [31]. The complex vectors for steady-state and small-signal upper-arm currents  $\mathbf{i}_u^0$  and  $\mathbf{i}_u$  are expressed in (2) with each element as the corresponding Fourier coefficient.

$$\begin{cases}
 \mathbf{i}_u^0 = [I_u^{-3} \ I_u^{-2} \ I_u^{-1} \ I_u^0 \ I_u^1 \ I_u^2 \ I_u^3]^\top \\
 \mathbf{i}_u = [I_u^{p-3} \ I_u^{p-2} \ I_u^{p-1} \ I_u^p \ I_u^{p+1} \ I_u^{p+2} \ I_u^{p+3}]^\top
 \end{cases} \quad (2)$$

where the superscripts  $\pm 3, \pm 2, \pm 1, 0$  represent the variables corresponding to  $\pm 3f_1, \pm 2f_1, \pm f_1, 0$ , respectively; and superscripts  $p \pm 3, p \pm 2, p \pm 1$  represent the variables corresponding to  $f_p \pm 3f_1, f_p \pm 2f_1, f_p \pm f_1$ , respectively.

Other related variables can also be described in this manner. For the symmetrical three-phase circuit of the MMC, the small-signal model can be expressed by one phase using common mode-differential mode (CM-DM) notations for cur-

rents, the modulation index, and voltages as follows:

$$\begin{cases} \mathbf{y}_{kc} = (\mathbf{y}_{ku} + \mathbf{y}_{kl})/2 \\ \mathbf{y}_{kd} = (\mathbf{y}_{ku} - \mathbf{y}_{kl})/2 \end{cases} \quad (3)$$

where the subscripts  $c$  and  $d$  represent the CM and DM, respectively; and  $\mathbf{y}$  could be the vectors of modulation index, current, and voltage, respectively, i.e.,  $\mathbf{y} = \mathbf{m}$ ,  $\mathbf{i}$ , or  $\mathbf{u}$ .

Therefore, with the index of the upper/lower arm omitted, the small-signal model of (1) can be transformed into the frequency domain as:

$$\begin{cases} \mathbf{Z}_{lr} \mathbf{i}_c = \frac{\mathbf{u}_{dc}}{2} - \mathbf{u}_c \\ \mathbf{Z}_{lr} \mathbf{i}_d = \mathbf{v}_o - \mathbf{u}_d - \mathbf{u}_s \\ \mathbf{u}_c = \mathbf{M}_c \mathbf{u}_c^\Sigma + \mathbf{M}_d \mathbf{u}_d^\Sigma + \mathbf{U}_c^\Sigma \mathbf{m}_c + \mathbf{U}_d^\Sigma \mathbf{m}_d \\ \mathbf{u}_d = \mathbf{M}_c \mathbf{u}_d^\Sigma + \mathbf{M}_d \mathbf{u}_c^\Sigma + \mathbf{U}_c^\Sigma \mathbf{m}_d + \mathbf{U}_d^\Sigma \mathbf{m}_c \\ \mathbf{Y}_c \mathbf{u}_c^\Sigma = \mathbf{M}_c \mathbf{i}_c + \mathbf{I}_c \mathbf{m}_c + \mathbf{M}_d \mathbf{i}_d + \mathbf{I}_d \mathbf{m}_d \\ \mathbf{Y}_c \mathbf{u}_d^\Sigma = \mathbf{M}_d \mathbf{i}_c + \mathbf{I}_c \mathbf{m}_d + \mathbf{M}_c \mathbf{i}_d + \mathbf{I}_d \mathbf{m}_c \end{cases} \quad (4)$$

where  $\mathbf{v}_o = \mathbf{G}_o \mathbf{u}_d$  with  $G_o(6,6)=1$ ;  $\mathbf{M}_c$ ,  $\mathbf{M}_d$ ,  $\mathbf{U}_c^\Sigma$ ,  $\mathbf{U}_d^\Sigma$ ,  $\mathbf{I}_c$ , and  $\mathbf{I}_d$  are the Toeplitz matrices of the steady-state complex vectors  $\mathbf{m}_c$ ,  $\mathbf{m}_d$ ,  $\mathbf{u}_c^\Sigma$ ,  $\mathbf{u}_d^\Sigma$ ,  $\mathbf{i}_c$ , and  $\mathbf{i}_d$ , respectively; and  $\mathbf{Z}_{lr}$  and  $\mathbf{Y}_c$  are defined as [32]:

$$\begin{cases} \mathbf{Z}_{lr} = j2\pi L_{arm} \text{diag}(f_p + nf_1 + R_{arm}) \\ \mathbf{Y}_c = j2\pi \frac{C_m}{N} \text{diag}(f_p + nf_1) \end{cases} \quad (5)$$

### B. Small-signal Modeling Under AC-side Perturbation

The GFM control structure of both MMC is presented in Fig. 2, where  $P_{ref}$ ,  $Q_{ref}$ ,  $\omega_{ref}$ ,  $U_{dc,ref}$ ,  $u_{dref}$ ,  $u_{qref}$ , and  $|u_{ref}|$  are the references of active power, reactive power, angular frequency, DC voltage,  $d$ -axis voltage,  $q$ -axis voltage, and the magnitude of PCC voltage  $u_s$ , respectively;  $p$ ,  $q$ ,  $U_{dc}$ , and  $|u_s|$  are the output active power, reactive power, DC voltage, and the magnitude of the PCC voltage, respectively; and  $i_{dq}$  and  $i_{cdq}$  are the  $dq$  components of the PCC current and circulating current  $i_c$ , respectively. The outer loop includes active power control (APC), AC voltage control (AVC), DC voltage control (DVC), and reactive power control (RPC). The inner control structure is the same as that in [31] and it is not shown here for simplicity. The inner control structure includes circulating current suppression control (CCSC), as well as AC- and DC-side virtual impedance control for stability enhancement and modulation, respectively. Typically, a WFMMC under GFC-based power control maintains the frequency and AC voltage magnitude of WF ( $SW=1$ ), whereas the GSMC adopts GFC-based DC voltage control for DC voltage and reactive power regulation ( $SW=2$ ), as shown in Fig. 2.

The proportional integral (PI) controller for CCSC should first be tuned to ensure the inner stability of MMC [33], [34]. Harmonic transfer functions can then be used to tune the PI parameters for CCSC. The inertia  $J$  and damping coefficients  $D_p$  of GFM control are then determined according to the frequency support function. Then, for the GSMC, the additional PI controller  $PI_{dc}$  for DC voltage control can be approximately tuned according to the power loop of the GFM control for the two-level voltage source converter (TLVSC) with the equivalent DC-side capacitance of  $3C_m/N$  like the method in [15], as the inner stability is satisfied.

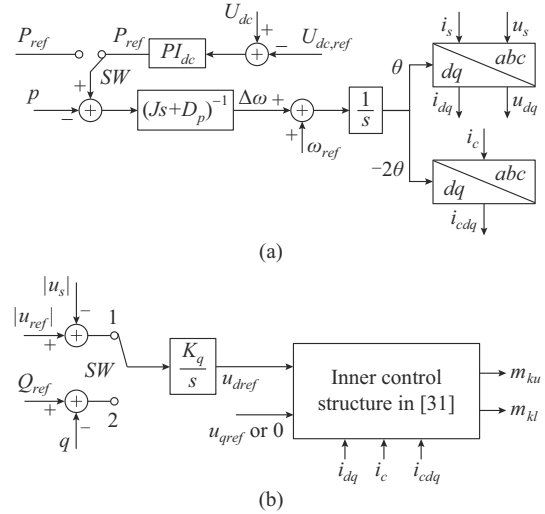


Fig. 2. GFC control structure of MMC. (a) APC. (b) RPC and inner control.

The effects of different DC voltage regulators on the VSM are discussed as in [34], and the impedance method in this study can be used for PI controller tuning of DC voltage. Similarly,  $k_q$  for the RPC and virtual impedance can be tuned. The complex vectors of CM modulation  $\mathbf{m}_c$  and DM modulation  $\mathbf{m}_d$  can be expressed as:

$$\begin{cases} \mathbf{m}_c = \mathbf{m}_{ci} + \mathbf{m}_{cvi} = \mathbf{Q}_c \mathbf{i}_c \\ \mathbf{m}_d^{pw} = \mathbf{m}_{dpv} + \mathbf{m}_{dpm} + \mathbf{m}_{dvi} + \mathbf{m}_{dmi} = (\mathbf{Q}_{pi} + \mathbf{Q}_{vi}) \mathbf{i}_d + (\mathbf{Q}_{pv} + \mathbf{G}_v) \mathbf{u}_s \\ \mathbf{m}_d^{dc} = \mathbf{m}_{dpv} + \mathbf{m}_{dpm} + \mathbf{m}_{dqv} + \mathbf{m}_{dmi} + \mathbf{m}_{dci} = (\mathbf{Q}_{pi} + \mathbf{Q}_{qi} + \mathbf{Q}_{vi}) \mathbf{i}_d + (\mathbf{Q}_{pv} + \mathbf{Q}_{qv}) \mathbf{u}_s + \mathbf{Q}_{dc} \mathbf{u}_{dc} \end{cases} \quad (6)$$

where the superscripts  $pw$  and  $dc$  represent the power control ( $SW=1$ ) and DC voltage control ( $SW=2$ ), respectively;  $\mathbf{Q}_c$  corresponds to CCSC and virtual impedance;  $\mathbf{Q}_{pi}$  and  $\mathbf{Q}_{pv}$  correspond to APC;  $\mathbf{Q}_{dc}$  corresponds to DVC;  $\mathbf{Q}_{qv}$  and  $\mathbf{Q}_{qi}$  correspond to RPC;  $\mathbf{G}_v$  corresponds to AVC; and  $\mathbf{Q}_{vi}$  corresponds to AC-side virtual impedance. In the  $\alpha\beta$  reference frame, the active and reactive power ( $p$  and  $q$ ) calculated by the PCC voltages ( $u_\alpha$ ,  $u_\beta$ ) and currents ( $i_\alpha$ ,  $i_\beta$ ) are expressed as:

$$\begin{cases} p = 1.5(i_\alpha u_\alpha + i_\beta u_\beta) \\ q = 1.5(i_\beta u_\alpha - i_\alpha u_\beta) \end{cases} \quad (7)$$

The PCC currents are twice the arm current in DM. Therefore, with current perturbation at the AC side, the active and reactive power (mainly of the frequency  $f_{p-1} = f_p - f_1$ ) in the small-signal complex vectors can be further expressed as:

$$\begin{cases} p = \mathbf{P}_i \mathbf{i}_d + \mathbf{P}_u \mathbf{u}_s + \mathbf{P}_{dc} \mathbf{u}_{dc} \\ q = \mathbf{R}_i \mathbf{i}_d + \mathbf{R}_u \mathbf{u}_s \\ P_i(3,2) = P_i^*(3,4) = 3U_s^1 \\ P_u(3,2) = P_u^*(3,4) = 1.5I_s^1 \\ P_{dc}(3,3) = -k_p^{dc} - k_i^{dc}/s_1 \\ R_i(3,2) = R_i^*(3,4) = -j3U_s^1 \\ R_u(3,2) = R_u^*(3,4) = 1.5I_s^1 \end{cases} \quad (8)$$

where  $k_p^{dc}$  and  $k_i^{dc}$  are proportional and integral coefficients, respectively; superscript \* denotes the conjugate operator, and  $s_1 = s - j2\pi f_1$ . Other elements of the matrices  $\mathbf{P}_i$ ,  $\mathbf{P}_u$ ,  $\mathbf{P}_{dc}$ ,  $\mathbf{R}_i$ , and  $\mathbf{R}_u$  that are not in (8) are 0. Furthermore, considering

the APC and DVC in Fig. 2, the phase-angle reference perturbation can be expressed as:

$$\theta = G_p(s_1)\mathbf{p} = -\frac{1}{s_1} \frac{1}{D_p + Js_1} (\mathbf{P}_i \mathbf{i}_d + \mathbf{P}_u \mathbf{u}_s + \mathbf{P}_{dc} \mathbf{u}_{dc}) \quad (9)$$

#### 1) APC and DVC

The effects of APC and DVC on the impedance have two aspects: the first is the park transformation (PT) effect on the reference voltage and the second is the effect of APC and DVC on the AC-side virtual impedance shaping. The reference voltage in the  $dq$  frame is  $[U_{dref}^0 \ 0]^T$ . After being transformed back to the  $abc$  frame, the perturbation in modulation  $m_{dpv}$  caused by phase angle can be expressed by inverse park transformation (IPT) with phase-shift  $\pi/2$  as:

$$\begin{bmatrix} \mathbf{u}_{aref} \\ \mathbf{u}_{bref} \\ \mathbf{u}_{cref} \end{bmatrix} = \mathbf{T}_{dq}^T (2\pi f_1 t + \pi/2) \theta_{p-1} \begin{bmatrix} U_{dref}^0 \\ 0 \end{bmatrix} \quad (10)$$

$$m_{dpv} = \frac{U_{dref}^0}{U_{dc}} \theta_{p-1} \sin(2\pi f_1 t) \quad (11)$$

where  $\mathbf{T}_{dq}^T$  is the PT matrix; and  $\theta_{p-1}$  is the phase angle of the frequency  $f_{p-1}$  in the time domain. Therefore, the perturbation caused by the phase-angle expressed in the complex vector form with  $G_p$  is expressed as:

$$\begin{cases} \mathbf{m}_{dpv} = G_p(s_1) \mathbf{G}_{pv} (\mathbf{P}_i \mathbf{i}_d + \mathbf{P}_u \mathbf{u}_s + \mathbf{P}_{dc} \mathbf{u}_{dc}) \\ G_{pv}(2, 3) = G_{pv}^*(4, 3) = \frac{jU_{dref}^0}{2U_{dc}} \end{cases} \quad (12)$$

The second effect concerns the APC and DVC on the AC-side virtual impedance control [34]. Here, the virtual inductance is analyzed, and the virtual resistance will be analyzed in a similar manner. The virtual inductance is implemented as:

$$\begin{cases} v_{dvi}(\omega) = -\frac{K_{vd}\tau_d S}{1 + \tau_d S} i_q(\omega) = -G_{hd}(s) i_{q\theta}(\omega) \\ v_{qvi}(\omega) = \frac{K_{vd}\tau_d S}{1 + \tau_d S} i_d(\omega) = G_{hd}(s) i_{d\theta}(\omega) \end{cases} \quad (13)$$

where  $i_d(\omega)$  and  $i_q(\omega)$  are the  $d$ - and  $q$ -axis small-signal perturbation currents in the frequency domain, respectively;  $K_{vd}$  and  $\tau_d$  are the gain and time constant of AC-side virtual impedance controller, respectively; and  $v_{dvi}(\omega)$  and  $v_{qvi}(\omega)$  are the voltage drop caused by  $i_q(\omega)$  and  $i_d(\omega)$ , respectively. The  $d$ - and  $q$ -axis current perturbations  $i_{d\theta}$  and  $i_{q\theta}$  caused by the PT with phase shift  $\pi/2$  are expressed as:

$$\begin{bmatrix} i_{d\theta} \\ i_{q\theta} \end{bmatrix} = \begin{bmatrix} I_q \\ -I_d \end{bmatrix} \theta_{p-1} = \mathbf{T}_{dq} (2\pi f_1 t + \pi/2) \begin{bmatrix} i_a \\ i_b \\ i_c \end{bmatrix} \theta_{p-1} \quad (14)$$

Therefore, (13) can be further simplified as:

$$\begin{bmatrix} v_{dvi}(\omega) \\ v_{qvi}(\omega) \end{bmatrix} = G_{hd}(s_1) \begin{bmatrix} I_d \\ I_q \end{bmatrix} \theta_{p-1}(\omega) \quad (15)$$

After the IPT, the modulation perturbation  $\mathbf{m}_{dpvi}$  of the virtual impedance caused by the APC and DVC can be obtained as:

$$\mathbf{m}_{dpvi} = G_{hd}(s_1) G_p(s_1) \mathbf{G}_{pvi} (\mathbf{P}_i \mathbf{i}_d + \mathbf{P}_u \mathbf{u}_s + \mathbf{P}_{dc} \mathbf{u}_{dc}) \quad (16)$$

$$|u_s| = \sqrt{u_d^2 + u_q^2} \approx (|U_s^1|^2 + 2|U_s^1||U_s^p| \cos(2\pi f_{p-1} t + \theta_s^p) + 2|U_s^1||U_s^{p-2}| \cos(2\pi f_{p-1} t + \theta_s^{p-2}))^{1/2} \approx |U_s^1| + |U_s^p| \cos(2\pi f_{p-1} t + \theta_s^p) + |U_s^{p-2}| \cos(2\pi f_{p-1} t + \theta_s^{p-2}) \quad (17)$$

where  $G_{pvi}(4, 3) = G_{pvi}^*(2, 3) = I_s^1/U_{dc}$ ;  $\theta_s^p = \text{ang}(U_s^p) - \text{ang}(U_s^1)$ ; and  $\theta_s^{p-2} = \text{ang}(U_s^{p-2}) - \text{ang}(U_s^1)$ .

#### 2) AVC for WFMMC

Similarly, for voltage control, the AC voltage perturbations are mainly of frequency  $f_p$  and  $f_{p-2}$ . Therefore,  $u_s$  only contains perturbation of frequency  $f_p - f_1$ , which can be further expressed as (17) with  $U_s^1$ ,  $U_s^p$ , and  $U_s^{p-2}$  as the Fourier coefficients of  $f_1$ ,  $f_p$ , and  $f_{p-2}$ . In addition, after the IPT, the modulation perturbations caused by the voltage control can be expressed as:

$$\begin{cases} u_{dref} = -\frac{K_q}{s_1} |u_s| \\ m_{dv} = \frac{-1}{U_{dc}} \cos(2\pi f_1 t) u_{dref} \\ \mathbf{m}_{dv} = \mathbf{G}_v(s_1) \mathbf{u}_s \\ G_v(2, 2) = G_v(4, 2) = \frac{K_q U_s^1}{2|U_s^1| U_{dc} s_1} \\ G_v(2, 4) = G_v(4, 4) = \frac{K_q U_s^{-1}}{2|U_s^{-1}| U_{dc} s_1} \end{cases} \quad (18)$$

where  $K_q$  is the integral coefficient of RPC.

#### 3) RPC for GSMMC

When  $SW=2$ , the reactive power is controlled and the corresponding modulation complex vector can be expressed as:

$$\begin{cases} \mathbf{u}_{dref} = -\frac{K_q}{s_1} \mathbf{q} = G_q(s_1) (\mathbf{R}_i \mathbf{i}_d + \mathbf{R}_u \mathbf{u}_s) \\ m_{dqv} = \frac{-1}{U_{dc}} \cos(2\pi f_1 t) U_{dref}^{p-1} \end{cases} \quad (19)$$

where  $U_{dref}^{p-1}$  is the  $d$ -axis small-signal perturbation of the voltage reference of frequency  $f_{p-1}$  in the time domain. The modulation perturbations caused by RPC  $\mathbf{m}_{dqv}$  can be expressed as:

$$\mathbf{m}_{dqv} = G_q(s_1) \mathbf{G}_{qv} (\mathbf{R}_i \mathbf{i}_d + \mathbf{R}_u \mathbf{u}_s) \quad (20)$$

where  $G_{qv}(2, 3) = G_{qv}(4, 3) = -1/(2U_{dc})$ .

#### 4) Virtual Impedance and CCSC

The harmonic transfer matrix of AC-side virtual inductance can be expressed as [34]:

$$\mathbf{m}_{di} = G_{hd}(s_1) \mathbf{G}_{di} \mathbf{i}_d \quad (21)$$

where  $G_{di}^*(2, 2) = G_{di}(4, 4) = j0.5/U_{dc}$ .

The DC-side virtual impedance can also be adopted, as in [34]. The DC-side virtual impedance for the CM current can be expressed as:

$$v_{cvi}(\omega) = -\frac{K_{vc}\tau_c S}{1 + \tau_c S} i_c(\omega) = G_{hc} i_c(\omega) \quad (22)$$

The modulation perturbation caused by the DC-side virtual impedance  $\mathbf{m}_{cvi}$  can be obtained as:

$$\mathbf{m}_{cvi} = \mathbf{G}_{cvi}(s) \mathbf{i}_c \quad (23)$$

where  $G_{cvi}(1, 1) = G_{hc}(s - j2\pi \times 3f_1)/U_{dc}$ ;  $G_{cvi}(3, 3) = G_{hc}(s -$

$j2\pi f_1)/U_{dc}$ ;  $G_{cvi}(5,5) = G_{hc}(s + j2\pi f_1)/U_{dc}$ ; and  $G_{cvi}(7,7) = G_{hc}(s + j2\pi \times 3f_1)/U_{dc}$ .

The modulation perturbation caused by CCSC  $\mathbf{m}_{ci}$  with the PI controller can be expressed as:

$$\mathbf{m}_{ci} = \mathbf{G}_{ci}(s)\mathbf{i}_c \quad (24)$$

where  $\mathbf{G}_{ci}$  is the circulating current controller,  $G_{ci}(1,1) = G_{ci}(5,5) = [k_p^c + k_i^c/(s - 2\pi f_1)]/U_{dc}$ , and  $G_{ci}(7,7) = [k_p^c + k_i^c/(s + 2\pi \times 5f_1)]/U_{dc}$ .

### C. AC- and DC-side Coupling

Considering the AC- and DC-side coupling, the DC- and AC-side perturbations  $\mathbf{u}_{dc}$  and  $\mathbf{u}_s$  can be expressed with the CM and DM currents, respectively, as:

$$\begin{cases} \mathbf{u}_{dc} = \mathbf{Z}_{dc}\mathbf{G}_{dc}\mathbf{i}_c \\ \mathbf{u}_s = \mathbf{Z}_{ac}\mathbf{G}_{ac}\mathbf{i}_d \end{cases} \quad (25)$$

where  $\mathbf{Z}_{dc}$  and  $\mathbf{Z}_{ac}$  are the DC- and AC-side impedance matrices in the frequency domain, respectively;  $G_{dc}(3,3) = -3$ ; and  $G_{ac}(2,2) = G_{ac}(4,4) = 2$ .

### D. Sequence Impedance

Equation (4) can be further simplified as:

$$\begin{cases} \mathbf{Z}_{lr}\mathbf{i}_c = \frac{\mathbf{u}_{dc}}{2} - \mathbf{u}_c \\ \mathbf{Z}_{lr}\mathbf{i}_d = \mathbf{v}_o - \mathbf{u}_d - \mathbf{u}_s \\ \mathbf{u}_c = \mathbf{B}_c\mathbf{i}_c + \mathbf{B}_d\mathbf{i}_d + \mathbf{C}_c\mathbf{m}_c + \mathbf{C}_d\mathbf{m}_d \\ \mathbf{u}_d = \mathbf{B}_d\mathbf{i}_c + \mathbf{B}_c\mathbf{i}_d + \mathbf{C}_d\mathbf{m}_c + \mathbf{C}_c\mathbf{m}_d \\ \mathbf{B}_c = \mathbf{M}_c\mathbf{Y}_c^{-1}\mathbf{M}_d + \mathbf{M}_d\mathbf{Y}_c^{-1}\mathbf{M}_c \\ \mathbf{B}_d = \mathbf{M}_c\mathbf{Y}_c^{-1}\mathbf{M}_c + \mathbf{M}_d\mathbf{Y}_c^{-1}\mathbf{M}_d \\ \mathbf{C}_c = \mathbf{M}_c\mathbf{Y}_c^{-1}\mathbf{I}_d + \mathbf{M}_d\mathbf{Y}_c^{-1}\mathbf{I}_c + \mathbf{U}_d^\Sigma \\ \mathbf{C}_d = \mathbf{M}_c\mathbf{Y}_c^{-1}\mathbf{I}_c + \mathbf{M}_d\mathbf{Y}_c^{-1}\mathbf{I}_d + \mathbf{U}_c^\Sigma \end{cases} \quad (26)$$

Next, based on the deduction of the modulation perturbation complex vector, the harmonic transfer matrices in DC voltage control mode can be summarized as:

$$\begin{cases} \mathbf{Q}_{id} = \mathbf{Q}_{pi} + \mathbf{Q}_{qi} + \mathbf{Q}_{vi} \\ \mathbf{Q}_v = \mathbf{Q}_{pv} + \mathbf{Q}_{qv} \\ \mathbf{G}_{icd} = 0.5\mathbf{Z}_{dc}\mathbf{G}_{dc} - \mathbf{Z}_{lr} - \mathbf{B}_d - \mathbf{C}_d\mathbf{Q}_c - \mathbf{C}_c\mathbf{Q}_{dc} \\ \mathbf{Q}_c = \mathbf{G}_{ci}(s) + \mathbf{G}_{cvi}(s) \\ \mathbf{Q}_{vi} = \mathbf{G}_{di}\mathbf{G}_{hd}(s_1) \\ \mathbf{Q}_{dc} = \mathbf{G}_p(s_1)\mathbf{P}_{dc}\mathbf{Z}_{dc}\mathbf{G}_{dc}(\mathbf{G}_{pv} + \mathbf{G}_{hd}(s_1)\mathbf{G}_{pvi}) \\ \mathbf{Q}_{pi} = \mathbf{G}_p(s_1)\mathbf{P}_i(\mathbf{G}_{pv} + \mathbf{G}_{hd}(s_1)\mathbf{G}_{pvi}) \\ \mathbf{Q}_{pv} = \mathbf{G}_p(s_1)\mathbf{P}_u(\mathbf{G}_{pv} + \mathbf{G}_{hd}(s_1)\mathbf{G}_{pvi}) \\ \mathbf{Q}_{qi} = \mathbf{G}_q(s_1)\mathbf{G}_{qv}\mathbf{R}_i \\ \mathbf{Q}_{qv} = \mathbf{G}_q(s_1)\mathbf{G}_{qv}\mathbf{R}_u \end{cases} \quad (27)$$

Note that in the power control mode,  $\mathbf{Q}_{id}$  and  $\mathbf{Q}_v$  in (27) are expressed in  $\mathbf{Q}_{id} = \mathbf{Q}_{pi} + \mathbf{Q}_{vi}$  and  $\mathbf{Q}_v = \mathbf{Q}_{pv} + \mathbf{G}_v$ . Then, with (6), (26), and (27) and with the modulation vectors eliminated, a detailed expression of the AC-side impedance can be expressed as [34]:

$$\mathbf{Z}_{mmc,ac} = -0.5 \frac{\mathbf{Z}_{lr} - (\mathbf{G}_o - \mathbf{E})(\mathbf{B}_d + \mathbf{C}_d\mathbf{Q}_{id}) - (\mathbf{G}_o - \mathbf{E})(\mathbf{B}_c + \mathbf{C}_c\mathbf{Q}_c + \mathbf{C}_d\mathbf{Q}_{dc})\mathbf{G}_{icd}^{-1}\mathbf{C}_c\mathbf{Q}_v + (\mathbf{G}_o - \mathbf{E})(\mathbf{B}_c + \mathbf{C}_c\mathbf{Q}_c + \mathbf{C}_d\mathbf{Q}_{dc})\mathbf{G}_{icd}^{-1}(\mathbf{B}_c + \mathbf{C}_c\mathbf{Q}_{id})}{(\mathbf{G}_o - \mathbf{E})\mathbf{C}_d\mathbf{Q}_v - \mathbf{E}} \rightarrow \leftarrow \quad (28)$$

The impedance shaping coupling effects of GFC are summarized in Table II [31]. For the DC voltage control and power control modes, the difference is reflected by  $\mathbf{Q}_{id}$  and  $\mathbf{Q}_v$  as well as  $\mathbf{Q}_{dc}$  in (27).

TABLE II  
IMPEDANCE SHAPING COUPLING EFFECTS OF GFC

Impedance	Control strategy	Perturbation feedback	Detailed expression	Modulation perturbations
AC-side impedance	RPC	$\mathbf{u}_s, \mathbf{i}_d$	$\mathbf{Q}_{qv}\mathbf{u}_s + \mathbf{Q}_{qi}\mathbf{i}_d$	
	AVC	$\mathbf{u}_s$	$\mathbf{G}_v\mathbf{u}_s$	
	APC and DVC (voltage reference)			$\mathbf{m}_d$
	APC and DVC (AC-side virtual impedance coupling)	$\mathbf{u}_s, \mathbf{i}_d, \mathbf{i}_c$	$\mathbf{Q}_{pv}\mathbf{u}_s + \mathbf{Q}_{pi}\mathbf{i}_d + \mathbf{Q}_{dc}\mathbf{i}_c$	
	AC-side virtual impedance	$\mathbf{i}_d$	$\mathbf{Q}_{vi}\mathbf{i}_d$	
DC-side impedance	DC-side virtual impedance	$\mathbf{i}_c$	$\mathbf{Q}_c\mathbf{i}_c$	$\mathbf{m}_c$
	CCSC			
	RPC	$\mathbf{i}_d$	$\mathbf{Q}_{qi}\mathbf{i}_d$	
	AVC		$\mathbf{G}_v\mathbf{Z}_{ac}\mathbf{i}_d$	
	APC and DVC (voltage reference)			$\mathbf{m}_d$
APC and DVC (AC-side virtual impedance coupling)	$\mathbf{i}_d, \mathbf{u}_{dc}, \mathbf{i}_c$	$\mathbf{Q}_{pi}\mathbf{i}_d + \mathbf{Q}_{dc}\mathbf{u}_{dc}$		
DC-side impedance	AC-side virtual impedance	$\mathbf{i}_d$	$\mathbf{Q}_{vi}\mathbf{i}_d$	
	DC-side virtual impedance	$\mathbf{i}_c$	$\mathbf{Q}_c\mathbf{i}_c$	$\mathbf{m}_c$
	CCSC			

### E. Small-signal Modeling for DC-side Impedance

According to Table II, the DC-side impedance is simpler because it consists of fewer elements caused by perturbations. For the DC-side impedance, (6) can be rewritten as:

$$\begin{cases} \mathbf{m}_c = \mathbf{m}_{ci} + \mathbf{m}_{cvi} = \mathbf{Q}_c\mathbf{i}_c \\ \mathbf{m}_d^{pv} = \mathbf{m}_{dpv} + \mathbf{m}_{dpvi} + \mathbf{m}_{dv} + \mathbf{m}_{di}(\mathbf{Q}_{pi} + \mathbf{Q}_{vi} + \mathbf{G}_v\mathbf{Z}_{ac})\mathbf{Q}_{id}\mathbf{i}_d \\ \mathbf{m}_d^{dc} = \mathbf{m}_{dpv} + \mathbf{m}_{dpvi} + \mathbf{m}_{dqv} + \mathbf{m}_{di} + \mathbf{m}_{dc}(\mathbf{Q}_{pi} + \mathbf{Q}_{qi} + \mathbf{Q}_{vi})\mathbf{i}_d + \mathbf{Q}_{dc}\mathbf{u}_{dc} = \mathbf{Q}_{id}\mathbf{i}_d + \mathbf{Q}_{dc} + \mathbf{u}_{dc} \end{cases} \quad (29)$$

Because AC voltage perturbations are dependent on the AC-side impedance and DM current, only the DM current is required for power calculations. The corresponding expressions of  $\mathbf{Q}_c$ ,  $\mathbf{Q}_{pv}$ ,  $\mathbf{Q}_{qi}$ ,  $\mathbf{Q}_{vi}$ , and  $\mathbf{Q}_{dc}$  for DC-side impedance can be expressed as:

$$\begin{cases} \mathbf{Q}_c = \mathbf{G}_{ci} + \mathbf{G}_{cvi} \\ \mathbf{Q}_{vi} = \mathbf{G}_{di} \mathbf{G}_{hd}(s) \\ \mathbf{Q}_{dc} = \mathbf{G}_p(s) \mathbf{P}_{dc} (\mathbf{G}_{pv} + \mathbf{G}_{pvi} \mathbf{G}_{hd}(s)) \\ \mathbf{Q}_{pi} = \mathbf{G}_p(s) (\mathbf{P}_i + \mathbf{P}_u \mathbf{Z}_{ac}) (\mathbf{G}_{pv} + \mathbf{G}_{hd}(s) \mathbf{G}_{pvi}) \\ \mathbf{Q}_{qi} = \mathbf{G}_q(s) \mathbf{G}_{qv} (\mathbf{R}_i + \mathbf{R}_u \mathbf{Z}_{ac}) \end{cases} \quad (30)$$

These definitions for DC-side impedance are similar to those for AC-side impedance, with some modifications. The DC-side impedance can be calculated as:

$$\mathbf{Y}_{mmc,dc} = 3 \frac{(0.5\mathbf{E} - \mathbf{C}_c \mathbf{Q}_{dc}) - (\mathbf{B}_c + \mathbf{C}_c \mathbf{Q}_{id}) \mathbf{G}_{icc}^{-1} (\mathbf{G}_o - \mathbf{E}) \mathbf{C}_d \mathbf{Q}_{dc}}{\mathbf{Z}_{lr} + \mathbf{B}_d + \mathbf{C}_d \mathbf{Q}_c + (\mathbf{B}_c + \mathbf{C}_c \mathbf{Q}_{id}) \mathbf{G}_{icc}^{-1} (\mathbf{G}_o - \mathbf{E}) (\mathbf{B}_c + \mathbf{C}_c \mathbf{Q}_c)} \quad (31)$$

$$\mathbf{G}_{icc} = \mathbf{Z}_{lr} + \mathbf{Z}_{ac} \mathbf{G}_{ac} - (\mathbf{G}_o - \mathbf{E}) (\mathbf{B}_d + \mathbf{C}_d \mathbf{Q}_{id}) \quad (32)$$

The DC-side impedance of an MMC with APC and DVC is obtained.

### III. VSC MODELING

The impedances of wind turbines with the GFM and GFL controls are presented to evaluate the interaction between the WF and MMC. The GFM and GFL control strategies of a wind turbine inverter are shown in Fig. 3. The grid-side converter of a wind turbine is considered here to evaluate the impedances, and the DC voltage can be constant because the DC side of the Type-IV wind turbine is equipped with relatively large capacitors [26], [27], [30].

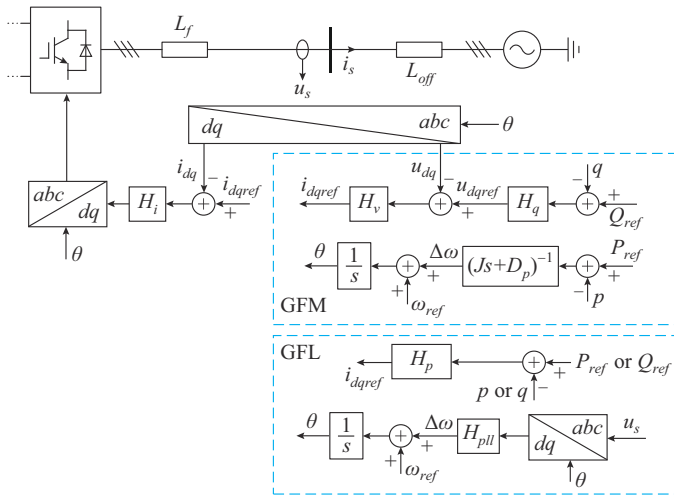


Fig. 3. GFL and GFM control strategies of wind turbine inverter.

The power stage of the two-level converter is simple as:

$$sL_f i = K_m U_{dc} m - u_s \quad (33)$$

where  $m$  is the modulation signal, which is the output of the current controller; and  $K_m$  is the gain of the converter. Injecting a positive-sequence voltage disturbance at the frequency  $f_p$  into the grid-tied converter system generates positive- and negative-sequence current/modulation responses at frequen-

cies  $f_p(i_p, m_p)$  and  $f_p - 2f_1(i_n, m_n)$ . Regardless of the GFM- or GFL-based control, the modulation signal can be influenced by current and voltage perturbations through the outer power/voltage and current controller as well as the synchronization unit. Therefore, the expression in the frequency domain can be summarized as:

$$\begin{cases} \mathbf{m}_p = -(\mathbf{A}_p \mathbf{u}_p + \mathbf{B}_p \mathbf{i}_p + \mathbf{C}_p \mathbf{i}_n) \\ \mathbf{m}_n = -(\mathbf{A}_n \mathbf{u}_p + \mathbf{B}_n \mathbf{i}_p + \mathbf{C}_n \mathbf{i}_n) \end{cases} \quad (34)$$

where  $\mathbf{m}_p$  and  $\mathbf{m}_n$  are the positive- and negative-sequence small-signal modulation signals, respectively;  $\mathbf{u}_p$ ,  $\mathbf{i}_p$ , and  $\mathbf{i}_n$  are the voltage and current perturbations in the frequency domain; and  $\mathbf{A}_p$ ,  $\mathbf{A}_n$ ,  $\mathbf{B}_p$ ,  $\mathbf{B}_n$ ,  $\mathbf{C}_p$ , and  $\mathbf{C}_n$  are the coefficients of the current and voltage perturbations.

According to (33) and (34), the admittances of wind turbine with the GFL and GFM controls can be expressed as (35) in a uniform manner.

$$\begin{cases} \mathbf{Y}_p = -\frac{i_p}{u_p} = \frac{K_m^2 U_{dc}^2 A_n C_p - (K_m U_{dc} A_p + 1)(sL_f + K_m U_{dc} C_n)}{K_m^2 U_{dc}^2 B_n C_p - (sL_f + K_m U_{dc} B_p)(s_2 L_f + K_m U_{dc} C_n)} \\ \mathbf{J}_p = -\frac{i_n}{u_p} = \frac{K_m U_{dc} A_n - K_m U_{dc} B_n Y_p}{s_2 L_f + K_m U_{dc} C_n} \end{cases} \quad (35)$$

#### A. Impedance of Wind Turbine with GFM Control

For GFM control, the coefficients  $\mathbf{A}_p$ ,  $\mathbf{A}_n$ ,  $\mathbf{B}_p$ ,  $\mathbf{B}_n$ ,  $\mathbf{C}_p$ , and  $\mathbf{C}_n$  include three parts. The first part is directly from the voltage/current control; the second one is from the coupling between the synchronization unit and voltage/current control; and the third one derives from RPC. The first part of coefficients derived from the voltage/current control can be expressed as:

$$\begin{cases} \mathbf{A}_{p1} = H_v(s_1) H_i(s_1), \mathbf{B}_{p1} = H_i(s_1), \mathbf{C}_{p1} = 0 \\ \mathbf{A}_{n1} = 0, \mathbf{B}_{n1} = 0, \mathbf{C}_{n1} = H_i(s_1) \end{cases} \quad (36)$$

where  $H_v$  and  $H_i$  are the voltage and current controllers, respectively. Next, the second part of coefficients is related to the equilibrium points of voltage, current, and modulation in the frequency domain and perturbation of the system phase  $\theta$  caused by voltage and current perturbations derived from the APC and DVC.

$$\begin{cases} \theta = -\frac{1}{s_1 (D_p + Js_1)} \mathbf{p} = \mathbf{G}_p(s_1) \mathbf{p} \\ \mathbf{p} = 3(I_s^{-1} \mathbf{u}_p + U_s^{-1} \mathbf{i}_p + U_s^1 \mathbf{i}_n) \end{cases} \quad (37)$$

Thus, the second part of coefficients derived from APC and DVC synchronization can be expressed as:

$$\begin{cases} \mathbf{A}_{p2} = -j1.5 I_s^{-1} G_p(s_1) [(I_s^1 + U_s^1 H_v(s_1)) H_i(s_1) + M^1] \\ \mathbf{B}_{p2} = -j1.5 U_s^{-1} G_p(s_1) [(I_s^1 + U_s^1 H_v(s_1)) H_i(s_1) + M^1] \\ \mathbf{C}_{p2} = -j1.5 U_s^1 G_p(s_1) [(I_s^1 + U_s^1 H_v(s_1)) H_i(s_1) + M^1] \\ \mathbf{A}_{n2} = j1.5 I_s^{-1} G_p(s_1) [(I_s^{-1} + U_s^{-1} H_v(s_1)) H_i(s_1) + M^{-1}] \\ \mathbf{B}_{n2} = j1.5 U_s^{-1} G_p(s_1) [(I_s^{-1} + U_s^{-1} H_v(s_1)) H_i(s_1) + M^{-1}] \\ \mathbf{C}_{n2} = j1.5 U_s^1 G_p(s_1) [(I_s^{-1} + U_s^{-1} H_v(s_1)) H_i(s_1) + M^{-1}] \end{cases} \quad (38)$$

The third part of coefficients derived from RPC can be similarly obtained as:

$$\begin{cases} \mathbf{u}_{dref} = H_q \mathbf{q} = 3H_q (-jI_s^{-1} \mathbf{u}_p + jU_s^{-1} \mathbf{i}_p - jU_s^{-1} \mathbf{i}_n) \\ A_{p3} = A_{n3} = -j1.5I_s^{-1} G_q(s_1) H_v(s_1) H_i(s_1) \\ B_{p3} = B_{n3} = j1.5U_s^{-1} G_q(s_1) H_v(s_1) H_i(s_1) \\ C_{p3} = C_{n3} = -j1.5U_s^{-1} G_q(s_1) H_v(s_1) H_i(s_1) \end{cases} \quad (39)$$

The modulation perturbations can be obtained by adding the three parts of coefficients as:

$$\begin{cases} A_p = \sum_{k=1}^3 A_{pk}, A_n = \sum_{k=1}^3 A_{nk} \\ B_p = \sum_{k=1}^3 B_{pk}, B_n = \sum_{k=1}^3 B_{nk} \\ C_p = \sum_{k=1}^3 C_{pk}, C_n = \sum_{k=1}^3 C_{nk} \end{cases} \quad (40)$$

### B. Impedance of Wind Turbine with GFL Control

The impedance of wind turbine with the GFL control can also be classified into three categories: current control effect, PLL effect, and power control effect. The first effect derived from the current control can be expressed as:

$$\begin{cases} A_{p1} = 0, B_{p1} = H_i(s_1), C_{p1} = 0 \\ A_{n1} = 0, B_{n1} = 0, C_{n1} = H_i(s_1) \end{cases} \quad (41)$$

The PLL effect can be expressed as:

$$\begin{cases} \boldsymbol{\theta} = \frac{-jH_{pll}(s_1)}{s_1 + |U_s|H_{pll}(s_1)} \mathbf{u}_p = -jG_{pll}(s_1) \mathbf{u}_p \\ A_{p2} = -0.5G_{pll}(s_1) [(I_s^{-1} + U_s^{-1} H_v(s_1)) H_i(s_1) + M^{-1}] \\ A_{n2} = 0.5G_{pll}(s_1) [(I_s^{-1} + U_s^{-1} H_v(s_1)) H_i(s_1) + M^{-1}] \\ B_{p2} = C_{p2} = B_{n2} = C_{n2} = 0 \end{cases} \quad (42)$$

where  $H_{pll}(s_1)$  corresponds to the PI controller of PLL for wind turbine.

The third effect can be expressed as follows. According to (37) and (39), the perturbations caused by the power can be rearranged as:

$$\begin{bmatrix} \mathbf{p} \\ -\mathbf{q} \end{bmatrix} = I_s^{-1} \begin{bmatrix} 1 \\ j \end{bmatrix} \mathbf{u}_p + U_s^{-1} \begin{bmatrix} 1 \\ -j \end{bmatrix} \mathbf{i}_p + U_s^{-1} \begin{bmatrix} 1 \\ j \end{bmatrix} \mathbf{i}_n \quad (43)$$

Therefore, the perturbation after PT can be expressed as:

$$\begin{cases} A_{p3} = C_{p3} = B_{n3} = 0, B_{p3} = U_s^{-1} H_p H_i \\ A_{n3} = I_s^{-1} H_p H_i, C_{n3} = U_s^{-1} H_p H_i \end{cases} \quad (44)$$

Finally, according to (40), the admittance can be obtained as in (35). Therefore, the impedance and admittance of the GFM- and GFL-controlled WF-based TLVSC are obtained as:

$$\mathbf{Z}_{wt} = \mathbf{Y}_{wt}^{-1} = \begin{bmatrix} Y_p(s) & J_p^*(2f_1 - s) \\ J_p(s) & Y_p^*(2f_1 - s) \end{bmatrix}^{-1} \quad (45)$$

where  $Y_p$  is the positive admittance; and  $J_p$  is the coupling term.

## IV. IMPEDANCE VERIFICATION

The detailed parameters of MMC-HVDC and WF are presented in Table III. In this section, the impedance of MMC without considering the WF is presented to verify the accuracy

of the MMC. In addition, the impedances of the GFL- and GFM-based wind turbine inverter are also provided.

TABLE III  
DETAILED PARAMETERS OF MMC-HVDC AND WF

System	Quantity	Value
MMC-HVDC	AC voltage	$U_s = 320$ kV
	DC rated voltage	$U_{dc} = 640$ kV
	Rated active power	$P_{ref} = 800$ MW
	Submodule capacitance	$C_m = 7000$ $\mu$ F
	Arm inductance	$L_{arm} = 40$ mH
	Number of SMs	$N = 288$
	Circulating current controller	$k_p^c = 20, k_i^c = 2000$
	DC voltage controller	$k_p^{dc} = 20, k_i^{dc} = 50$
	Frequency response controller	$k_{dc}^i = 20, k_{dc}^r = 5, T_d = 0.005$ s
	Reactive power controller	$k_q = 4$
	Active power controller	$D_p = 20, J = 0$
	DC voltage control	$D_p = 20, J = 0$
	AC-side virtual impedance (70° or 90°)	$k_{vd} = 10, \tau_d = 0.1$ s
	DC-side virtual impedance	$k_{vc} = 10, \tau_c = 0.1$ s
Grid-side line impedance	$L_{on} = 0.15$ H	
WF-side line impedance	$L_{off} = 0.12$ H	
Arm equivalent resistance	$R_{arm} = 1$ $\Omega$	
WF	AC voltage	$U_s = 0.69$ kV
	DC rated voltage	$U_{dc} = 1.5$ kV
	Rated active power	$P_{ref} = 5$ MW
	Number of wind turbines	$N_{wt} = 160$
	Filter inductance	$L_f = 200$ $\mu$ H
	Converter gain	$K_m = 0.5$
	Current controller (GFL)	$k_p^i = 1, k_i^i = 50$
	Current controller (GFM)	$k_p^i = 1, k_i^i = 10$
	Voltage controller	$k_p^v = 1, k_i^v = 10$
	PLL	$k_p^{pll} = 1000, k_i^{pll} = 5000$
Power controller (GFL)	$k_p^p = 1, k_i^p = 10$	
Reactive power controller	$k_p^q = 0.5, k_i^q = 1$	
Active power controller	$D_p = 5$	

### A. GSMC and WFMMC

The GSMC and WFMMC based on DVC and APC are presented, respectively. As shown in Fig. 4(a), the sequence impedances of GSMC and WFMMC including AC-side virtual impedance are nearly the same, with trivial differences derived from the DC voltage controller. The DC-side impedances of GSMC (with AC-side virtual impedance of 70°) and WFMMC (with AC-side virtual impedance of 90°) are shown in Fig. 4(b). Overall, the analytical result matches the measurements well. The main influence range of GFM control is within 200 Hz. The coupling terms should be considered using the generalized Nyquist criterion (GNC). In addition, as shown in Fig. 4(c), with the DC- or AC-side virtual impedance (90°) in Table III, the DC-side impedance of the WFMMC is damped to a certain degree as compared with that without virtual impedance. The damping effect of the AC-side virtual impedance is significant, as the negative-

resistance region is minimized with the AC-side virtual impedance ( $90^\circ$ ). Furthermore, if the AC-side virtual impedance ( $70^\circ$ ), where the gains of high-pass filters of virtual inductance and resistance are  $k_{vd}\sin(70^\circ)$  and  $k_{vd}\cos(70^\circ)$ , respectively, is implemented as in the GSMMC, the negative-resistance region can be eliminated as compared with the pure virtual inductance ( $90^\circ$ ) for the GSMMC [34].

### B. GFL-/GFM-based Wind Turbine

The GFL and GFM control strategies shown in Fig. 3 for the Type-IV wind turbine can be implemented with the admittance shown in Fig. 5. The admittance of the Type-IV wind turbine has a resonant peak at approximately 50 Hz, and the coupling terms are apparent and cannot be overlooked with GFL. In addition, the GFM control features a low magnitude of approximately 50 Hz for the positive sequence, whereas the coupling terms are at their highest magnitude at approximately 50 Hz, as shown in Fig. 5(b). The coupling terms of the GFM and GFL control both feature a high magnitude, and the GNC should be used for stability analysis. Overall, the impedance model corresponds with the impedance measurements.

## V. CASE STUDIES

This section presents three case studies to demonstrate the stability effects of different WF control strategies on the AC- and DC-side stabilities and describes the grid-supporting function provided to the receiving-end grid by the GFM-based WF with the modified GFM control for the MMC. It is noteworthy that the main focus of this study is on a relatively weak grid situation with a larger line impedance.

### A. Effects of WF on DC-side Impedance of WFMMC

The DC-side impedance of the WFMMC can be obtained using (31), with the impedance of the WF from (45), i.e.,  $K_t^2 \mathbf{Z}_{wt}/N_{wt}$ . In addition, to better show the effects of WF on the DC-side impedance of WFMMC, (26) can be simplified as:

$$\begin{cases} \mathbf{E}_c \mathbf{i}_d + \mathbf{F}_c \mathbf{i}_c = \mathbf{G}_c \mathbf{u}_s + \mathbf{H}_c \mathbf{u}_{dc} \\ \mathbf{E}_d \mathbf{i}_d + \mathbf{F}_d \mathbf{i}_c = \mathbf{G}_d \mathbf{u}_s + \mathbf{H}_d \mathbf{u}_{dc} \\ \mathbf{E}_d = \mathbf{Z}_{lr} - (\mathbf{G}_o - \mathbf{E})(\mathbf{B}_c + \mathbf{C}_c \mathbf{Q}_{id}) \\ \mathbf{E}_c = \mathbf{B}_d + \mathbf{C}_d \mathbf{Q}_{id} \\ \mathbf{F}_d = (\mathbf{E} - \mathbf{G}_o)(\mathbf{B}_d + \mathbf{C}_d \mathbf{Q}_c + \mathbf{C}_c \mathbf{Q}_{ic}) \\ \mathbf{F}_c = \mathbf{Z}_{lr} + \mathbf{B}_c + \mathbf{C}_c \mathbf{Q}_c + \mathbf{C}_d \mathbf{Q}_{ic} \\ \mathbf{G}_c = -\mathbf{C}_d \mathbf{Q}_v \\ \mathbf{G}_d = (\mathbf{G}_o - \mathbf{E})\mathbf{C}_c \mathbf{Q}_v - \mathbf{E} \\ \mathbf{H}_c = 0.5\mathbf{E} - \mathbf{C}_d \mathbf{Q}_{dc} \\ \mathbf{H}_d = (\mathbf{G}_o - \mathbf{E})\mathbf{C}_c \mathbf{Q}_{dc} \end{cases} \quad (46)$$

$$\begin{cases} \mathbf{i}_c = \mathbf{Y}_{da} \mathbf{u}_s + \mathbf{Y}_{dcs} \mathbf{u}_{dc} \\ \mathbf{i}_d = \mathbf{Y}_{acs} \mathbf{u}_s + \mathbf{Y}_{ad} \mathbf{u}_{dc} \\ \mathbf{Y}_{da} = (\mathbf{F}_c - \mathbf{E}_c \mathbf{E}_d^{-1} \mathbf{F}_d)^{-1} (\mathbf{G}_c - \mathbf{E}_c \mathbf{E}_d^{-1} \mathbf{G}_d) \\ \mathbf{Y}_{dcs} = (\mathbf{F}_c - \mathbf{E}_c \mathbf{E}_d^{-1} \mathbf{F}_d)^{-1} (\mathbf{H}_c - \mathbf{E}_c \mathbf{E}_d^{-1} \mathbf{H}_d) \\ \mathbf{Y}_{acs} = \mathbf{E}_d^{-1} \mathbf{G}_d - \mathbf{E}_d^{-1} \mathbf{F}_d \mathbf{Y}_{da} \\ \mathbf{Y}_{ad} = \mathbf{E}_d^{-1} \mathbf{H}_d - \mathbf{E}_d^{-1} \mathbf{F}_d \mathbf{Y}_{dcs} \end{cases} \quad (47)$$

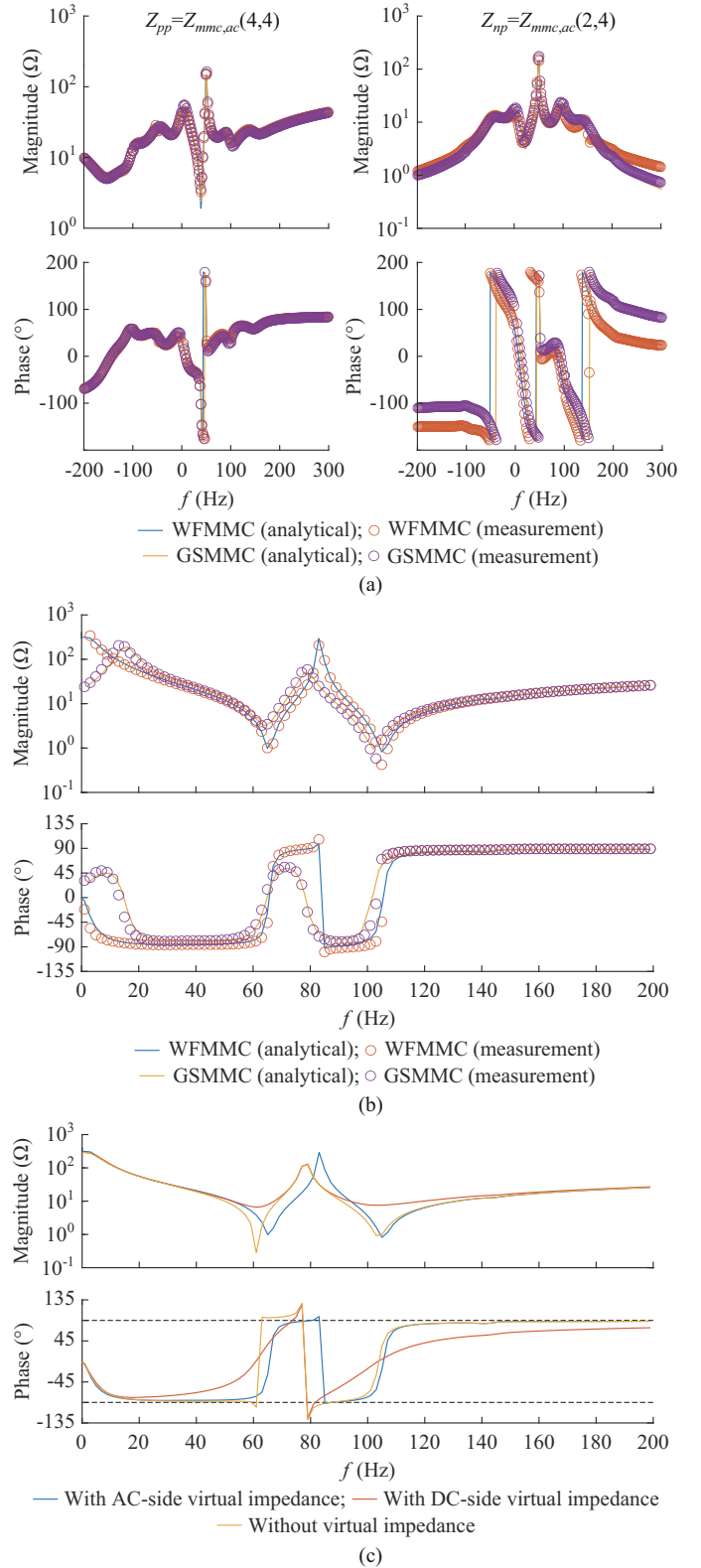


Fig. 4. Impedances of GFM-based MMC. (a) Sequence impedances. (b) DC-side impedances. (c) DC-side impedance of WFMMC with or without virtual impedance.

Note that  $\mathbf{Y}_{acs}$  and  $\mathbf{Y}_{dcs}$  are the admittances of MMC when connected to the ideal DC and AC voltages, respectively, without AC- and DC-side coupling. Therefore, (46) and (47) are simplified as compared with (28) and (31), respectively.

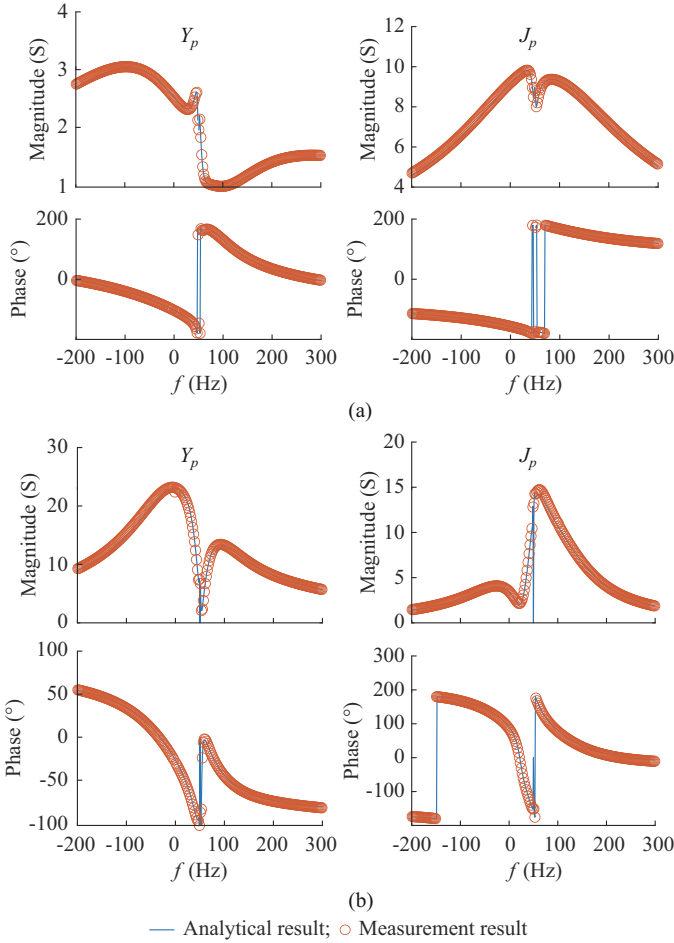


Fig. 5. Admittance of wind turbine with GFL and GFM controls. (a) GFL control. (b) GFM control.

However, they are suitable for analyzing the coupling between the AC and DC sides under non-ideal AC and DC grids.  $Y_{ad}$  and  $Y_{da}$  are the coupling terms from DC to AC and from AC to DC sides, respectively. According to (47), when  $\mathbf{u}_s = \mathbf{Z}_{ac} \mathbf{G}_{ac} \mathbf{i}_d$  is considered, (48) can be obtained.

$$\mathbf{i}_{dc} = 3 \left( \mathbf{Y}_{dcs} + \frac{\mathbf{Y}_{da} \mathbf{Z}_{ac} \mathbf{G}_{ac} \mathbf{Y}_{ad}}{\mathbf{E} - \mathbf{Y}_{acs} \mathbf{Z}_{ac} \mathbf{G}_{ac}} \right) \mathbf{u}_{dc} \quad (48)$$

From (48), it can be observed that the DC-side admittance consists of two parts: self-admittance and the coupling term from the AC to the DC sides. In addition, when the AC-side impedance is considered with  $\mathbf{Z}_{ac} = \mathbf{Z}_{Loff} = j\omega \mathbf{L}_{off}$ , (48) is equivalent to (31). Furthermore, when the WF is integrated, the equivalent grid impedance changes to  $\mathbf{Z}_{ac} = \mathbf{Z}_{Loff} + \mathbf{Z}_{wt} K_t^2 / N_{wt}$ . Therefore, it is possible to effectively shape the DC-side impedance of the WFMMC with WF integration owing to its impedance  $\mathbf{Z}_{wt}$ . Thus, it is natural that it can shape the DC-side impedance of the MMC by mapping the admittance as  $3\mathbf{Y}_{da} \mathbf{Z}_{ac} \mathbf{G}_{ac} \mathbf{Y}_{ad} / (\mathbf{E} - \mathbf{Y}_{acs} \mathbf{Z}_{ac} \mathbf{G}_{ac})$ . WF could have a positive damping effect on the DC-side impedance of the WFMMC because of mapping impedance.

When the GFL-based WF is connected to the WFMMC, the DC-side impedance is better damped as compared when it is not connected, as shown by the blue curve with AC-side virtual impedance in Fig. 4(b). The negative resistance

is well suppressed even without the virtual impedance, as indicated by the yellow curve in Fig. 6(a), which shows the stability improvement of the GFL-based WF-integrated system. The impedance of the WF, as well as the large feeder line, plays a critical role in the DC-side impedance of the WFMMC, with weak shaping effects of GFM on MMC. As shown in Fig. 6(a), a change in the number of GFL-based wind turbines  $N_{wt}^{GFL}$  from 120 to 160 has a minor effect on the DC-side impedance, whereas the current WF controller has an apparent effect on the impedance of MMC. For example, as shown in Fig. 6(a), when the proportional coefficient of the current controller drops from 1.0 to 0.1, the DC-side impedance changes. The DC-side stability is better when  $k_p^i = 0.1$ . In addition, the main oscillation modes are approximately 10 Hz and 70 Hz at the intersection frequencies of the GSMMC and WFMMC impedance curves, respectively. The phase margin of the GFL-based WF-integrated MMC-HVDC is shown in Fig. 6(a), and the phase differences of the main oscillation mode at approximately 70 Hz when two curves intersect are given in the legend according to the corresponding stability margin.

Regarding the GFM-based WF-integrated MMC-HVDC, the WF has a major effect on the DC-side impedance of the GFM-based MMC. However, slightly different from the GFL-based WF, the GFM-based WF has a relatively better damping effect on the DC-side stability with a larger proportional coefficient current controller, as shown by the purple curve with  $k_p^i = 1$  in Fig. 6(b). For example, with  $k_p^i = 1$ , the DC-side impedance of the WFMMC is better suppressed with a better stability margin as compared with the GFL control strategy. By contrast, it is reversed with  $k_p^i = 0.1$ , as shown in Fig. 6(b).

To show the different effects of the GFM- and GFL-based WF on the DC-side stability of the MMC-HVDC, the parameters listed in Table III are adopted. Prior to  $t = 3$  s, the number of wind turbines is 120, the power is approximately 600 MW, and the DC current is approximately 0.95 kA. When  $t = 3$  s, the number of wind turbines increases to 160, and the total active power is approximately 800 MW, with a DC current of 1.25 kA. As can be observed in Fig. 6(c) and (d), the GFM-based WF outperforms the GFL-based WF with  $k_p^i = 1$ , whereas the GFL-based WF performs better with  $k_p^i = 0.1$ . This corresponds to the impedance-shaping effects of the WF. As shown in Fig. 6(c) and (d), the DC-side virtual impedance stabilizes the system.

### B. AC-side Impedance and Stability of WFMMC

The AC-side impedance of the WFMMC can be obtained by substituting the DC-side impedance of the GSMMC from (31) to (28). The AC-side impedance of GSMMC can also be obtained by substituting the DC-side impedance of WFMMC. In addition, the coupling from DC to AC side can be analyzed using the same method as the AC to DC-coupling analysis presented in the previous section and it is not repeated. As the grid-side stability of the GFM-based MMC has been thoroughly evaluated in our related work, the AC-side stability of WFMMC is the main focus here. Figure 7(a) shows the AC-side impedance of the WFMMC (with AC feeder line impedance) with the ideal and actual GSMMCs.

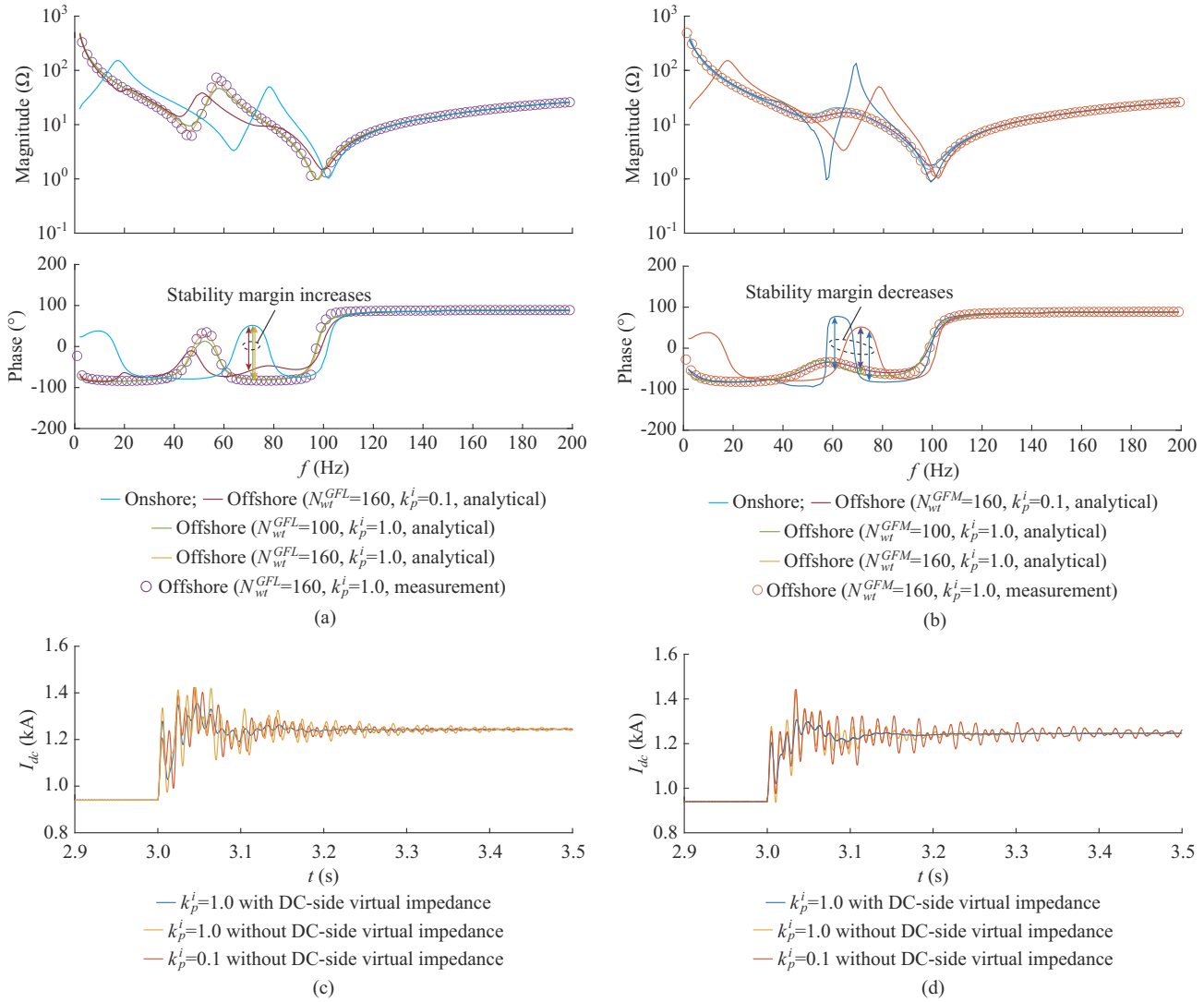


Fig. 6. Impedance of WF-integrated WFMDC and GSMDC. (a) DC-side impedance of GFL-based WF-integrated WFMDC without virtual impedance. (b) DC-side impedance of GFM-based WF-integrated WFMDC without virtual impedance. (c) DC-side current response of GFL-based WF. (d) DC-side current response of GFM-based WF.

The effect of GSMDC on the AC-side impedance of WFMDC including the feeder line is trivial, with only a slight decrease in the coupling terms. Considering the large coupling terms of WF shown in Fig. 5, the WF and WFMDC interactions should be studied using the GNC. The WF is the subsystem, whereas the line impedance together with the WFMDC represents the other subsystem. Therefore, the stability can be evaluated by the ratio between these two subsystems, i. e.,  $(\mathbf{Z}_{mmc,ac} + \mathbf{Z}_{Loff})\mathbf{Y}_{wt}N_{wt}/K_t^2$ . Here, the transformer and DC cable can be included using T and  $\pi$  equivalent circuits [35]. However, they are not the main focus of this study and thus are ignored.

The GFL-based WF is known to have poor performances in weak grids because of the PLL. Here, with WF integration, a different line impedance is used. As can be observed in Fig. 7(b), with the increase in line impedance, the allowable number of wind turbines is reduced or the bandwidth of the PLL is decreased to integrate all wind turbines with a relatively large line impedance. This shortage can be effectively attenuated using a GFM-based WF.

Using the GFM control, the wind turbine integration can always be stably maintained, as shown in the right portion of Fig. 7(b), with  $L_{off}=0.17$  H and  $k_p^{pll}=1500$ . The system begins to stabilize with 10 GFM-based wind turbines implemented of the total 160 wind turbines. Figure 7(b) shows that the combinations of GFM and GFL control strategies can ease the system stability. The stability can be accessed by the ratio  $[K_t^2(\mathbf{Z}_{mmc,ac} + \mathbf{Z}_{Loff})^{-1} + \mathbf{Y}_{wt}^{GFM}N_{wt}^{GFM}]^{-1}\mathbf{Y}_{wt}^{GFL}N_{wt}^{GFL}$ . In addition, with the increasing PLL bandwidth, the minimum number of GFM-based wind turbines should increase. Although it is a simple demonstration without considering right half plane poles, it reveals the benefits of GFM control for WFs in weak grids [36].

Figure 7(c) presents the power response of a GFL-based WF-integrated MMC-HVDC system with  $L_{off}=0.17$  H. When the proportional coefficient of PLL  $k_p^{pll}$  increases from 1000 to 1200 at  $t=3$  s, the system power begins to oscillate at approximately 180 Hz. After  $t=3.1$  s, 15 wind turbines switch to GFM control, and the system is stable again. This simulation corresponds to the analysis.

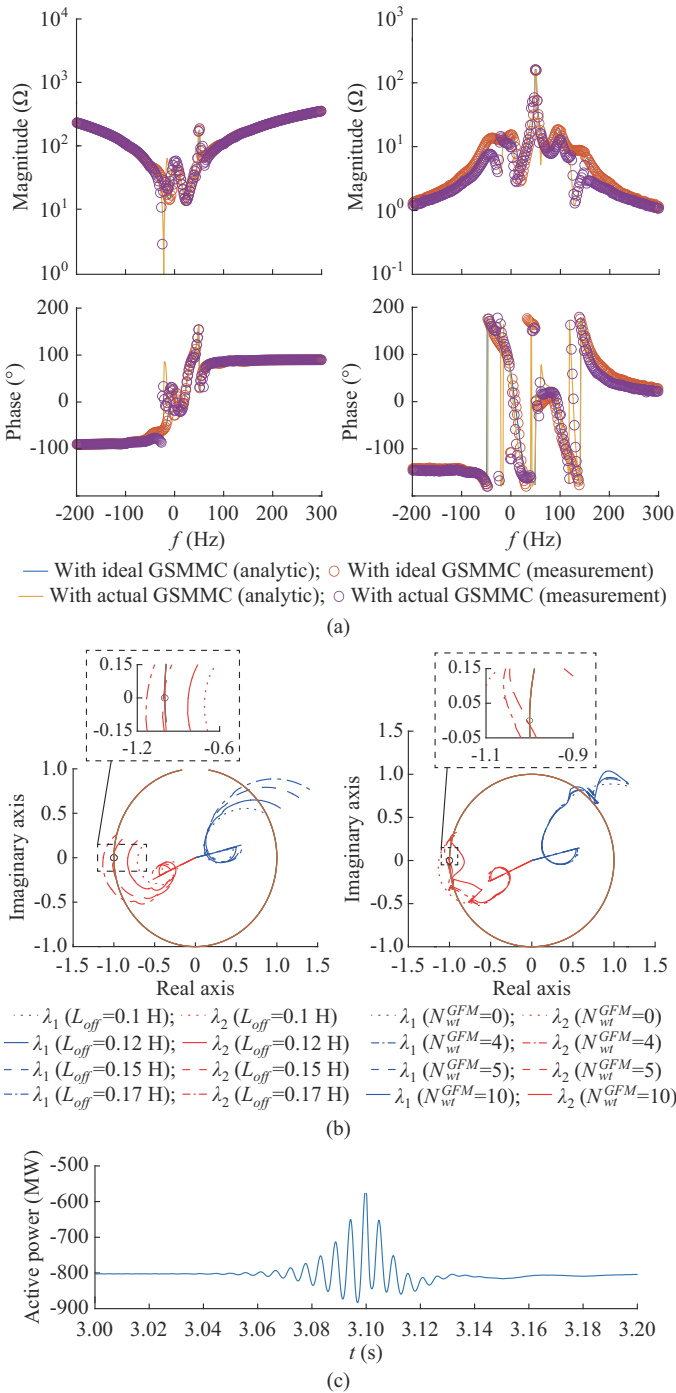


Fig. 7. AC-side stability of WFMMC and WF. (a) AC-side impedance of WFMMC with ideal and actual GSMMCs ( $L_{off}=0.17$  H,  $L_{on}=0.2$  H). (b) Nyquist plots. (c) Active power.

### C. Grid Supporting with GFM-based WF-integrated MMC-HVDC

The previous analysis shows that both WFs and MMC-HVDCs should adopt GFM control in weak grids. However, the GSMMC using DVC with a PI controller cannot effectively respond to the grid-side frequency excursion. Currently, the proposed coordination strategies for MMC-HVDCs and WFs for receiving-end AC system support can be classified into communication-based and communication-free strategies. In a communication-based strategy, the frequency in-

formation is transmitted to the WF by communication to provide the necessary support. However, the commutation-free strategies are preferable. With a communication-free strategy, the core problem is frequency transmission from the onshore grid to the offshore WF. As shown in Fig. 8(a), the onshore GSMMC adopts the frequency DC voltage droop control, and the offshore WFMMC adopts DC voltage frequency or AC voltage magnitude droop control. The WF can sense the frequency change of the onshore grid through the DC voltage and provide the necessary frequency support. Conventionally, both the GSMMC and WF use the PLL-based GFL control, whereas the WFMMC adopts voltage-frequency (VF) control. The GFL control may suffer from instability and a slow response due to the stability requirements of the PLL. In this section, a GFM-based coordination of the MMC-HVDC and WF is proposed for receiving-end grid frequency support.

To make the MMC-HVDC system respond to the AC grid, the GSMMC and WFMMC control strategies are revised according to Fig. 8(a), which is known as the Type-I control and is similar to the frequency response, as shown in Fig. 8(b). The GSMMC responds to the system frequency and exhibits a DC voltage deviation. This deviation is sensed and transformed into the system frequency deviation of the WFMMC. Then, the GFM-based WF can output more or less power based on the frequency deviation of the WFMMC. The DC voltage droop can be adjusted using  $K_{dc}^r$ , and the frequency droop can be adjusted using  $K_{dc}^i$ . A low-pass filter with  $T_d=0.005$  s is used to filter the noise in frequency. A similar control is presented in [29]; however, it is a DC voltage droop with an outer loop power feedback. In addition, instead of the GFM-based WF with a frequency response, the WF in [29] is based on GFL, as shown in Fig. 8(c).

If the WF is connected to a weak AC sending-end system, the WFMMC and GSMMC control can be switched (the sending end controls the DC voltage, and the receiving end controls the power) without modification, as shown in Fig. 1, to ensure the frequency support for the receiving-end system. This is known as Type-II control for frequency response. However, if the WF is islanded, using Type-I control is preferred when the WF cannot provide sufficient power to maintain the DC voltage.

Figure 8(d) shows the response of a WF-integrated MMC-HVDC system to grid-side frequency changes. After  $t=5$  s, the frequency drops to 49.85 Hz. After  $t=7$  s, the system frequency steps further to 49.7 Hz. Both Type-I and Type-II control strategies can respond well to grid frequency excursions. However, to a certain degree, the first strategy induces a DC voltage deviation of less than 5%, which is proportional to the grid frequency deviation that is usually within 1%. The second strategy features no DC voltage deviation within the WF power capacity and a shortage of voltage collapse if it is outside the WF power capabilities.

We conduct a further comparison with the coordination of conventional PLL-based GFL control strategy. For simplicity, the MMC-HVDC still uses the GFM control in a manner similar to the Type-I control, whereas the WF can adopt the

GFL-based control shown in Fig. 3 with the frequency support shown in Fig. 8(c).

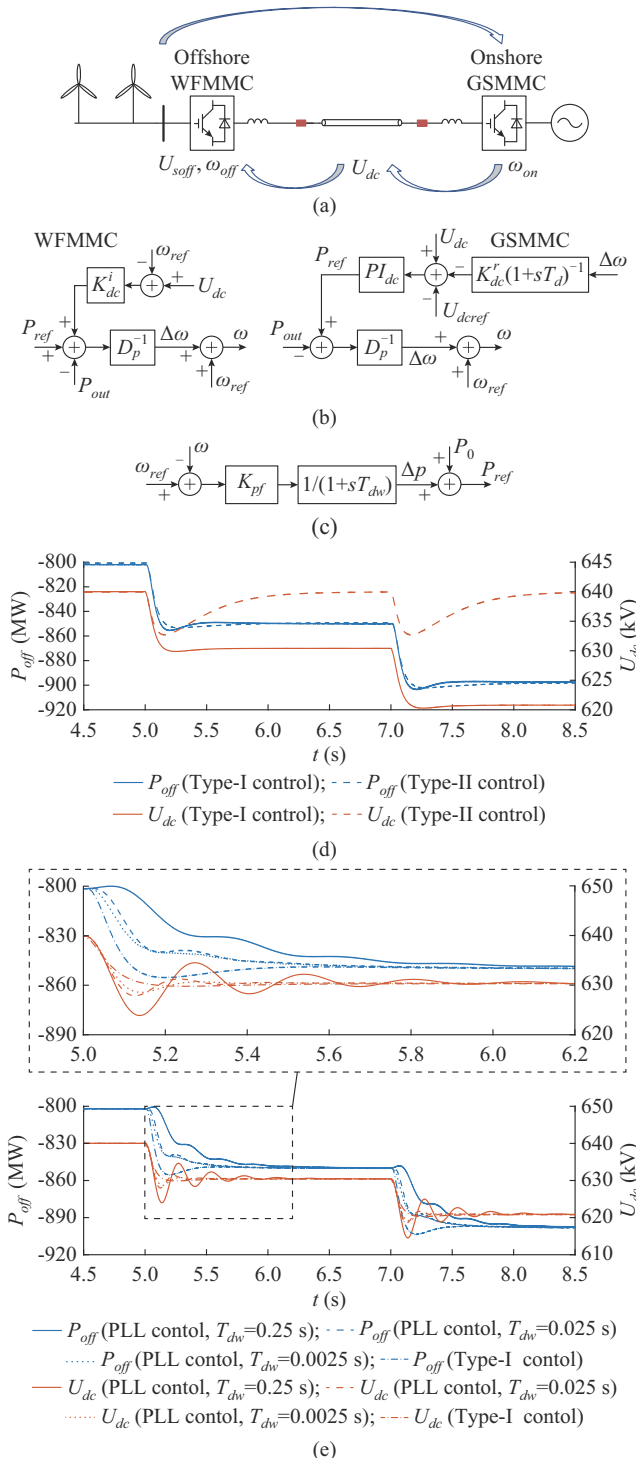


Fig. 8. Frequency support of WF-integrated MMC-HVDC. (a) Principle of communication-free coordination of WF-integrated MMC-HVDC. (b) Type-I control. (c) Ancillary frequency support for conventional GFL-based WF. (d) Response of WF-integrated MMC-HVDC system to grid-side frequency change. (e) Comparison of GFM- and GFL-based WFs.

To provide the same amount of active power with frequency excursion, the droop of GFL-based WF  $K_{pf}$  is 5, while the time constant  $T_{dw} \geq 0.0025$  s of the low-pass filter is necessary for noise filtering due to the stability requirement.

Three cases at  $T_{dw}=0.05$  s,  $T_{dw}=0.025$  s, and  $T_{dw}=0.0025$  s are tested under Type-I control for a detailed comparison. Figure 8(e) shows the comparisons of the GFL- and GFM-based WFs, which uses PLL control and Type-I control, respectively. Overall, the GFL- and GFM-based WFs could both provide the necessary frequency support. However, the response time of the GFM-based WF is shorter than that of the GFL-based WF, as shown in Fig. 8(e). Moreover, due to the slow response of the GFL-based WF when  $T_{dw}=0.25$  s, the DC voltage fluctuates and reaches a nadir, acting as an energy storage buffer to provide active power to the onshore GSMMC for grid support. Reducing the time constant of the low-pass filter can improve the response time and suppress the DC voltage fluctuation. However, the effect is limited by the risk of instability. Thus, the two proposed coordination strategies for the WF-integrated MMC-HVDC outperform the conventional GFL-based coordination method when considering fast frequency support and stability in a weak grid.

#### D. Comparison and Remarks

Table IV presents a better comparison of the GFL- and GFM-based WFs on the AC- and DC-side stabilities and the frequency support response. As previously analyzed, the GFL-based WF is preferable for the DC-side stability of a GFM-based MMC-HVDC with a smaller  $k_p^i$ , whereas a GFM-based WF is preferable with a larger  $k_p^i$ . Regarding the AC-side stability between the GSMMC and onshore grid, the GFM-based MMC-HVDC is thought to be suitable at  $SCR < 3$ . The AC-side stability between the WF and WFMMC also exhibit a similar phenomenon. When  $SCR < 3$  or  $L_{off} > 0.33$  p.u., using the GFM control for the WF is recommended. In addition, a GFM-based wind turbine can be used to enhance the overall WF stability. Considering the output impedance of the offshore WFMMC,  $SCR < 3$  or  $L_{off} > 0.33$  p.u. is approximate, and accurate stability analysis should employ the Nyquist criterion. Finally, for the frequency support function, the GFM-based WF outperforms the GFL-based WF.

TABLE IV  
COMPARISON OF GFL- AND GFM-BASED WFs ON AC- AND DC-SIDE STABILITIES AND FREQUENCY SUPPORT RESPONSE

Type	DC-side stability of MMC-HVDC	AC-side stability of GSMMC	AC-side stability of WFMMC	Frequency support
GFL-based WF	Damping increase with decrease of $k_p^i$	Instability	Instability	Slow response with worse stability
GFM-based WF	Damping increase with increase of $k_p^i$	Stability	Stability	Fast response with better stability

## VI. CONCLUSION

This study investigates the interaction and coordination of a GFM-based MMC-HVDC integrated with GFM/GFL-based WFs. First, the impedances of a GFM-based MMC and a WF with GFM and GFL control are derived. The influences of GFM- and GFL-based WFs on the DC- and AC-side stabilities of the GFM-based MMC-HVDC system is

then investigated by comparing the GFM- and GFL-based WFs in a weak grid integration. The GFM-based grid frequency support strategies are then proposed to support the receiving-end AC system in a weak grid.

The WF has a positive damping effect on the DC-side stability of the GFM-based MMC-HVDC system such that the virtual impedance is no longer important, and the effects are different under GFM and GFL control when considering the proportional coefficient. A larger and smaller proportional coefficient is better for the GFM- and GFL-based WF for the DC-side stability of the MMC-HVDC system, respectively.

Regarding the AC-side stability, the main causes of instability under WF integration in a weak grid are the interactions between the WFMMC- and GFL-based WFs by the PLL bandwidth. The GFM-based WF has no such instability and could thus be adopted in a WF to stabilize the system.

Finally, a GFM-based WF-integrated MMC-HVDC WF for receiving-end grid frequency support is proposed and verified through simulations. A comparison shows that the GFM-based WF outperforms the GFL-based WF in terms of stability and response speed. As a future research direction, network-based system stability with a GFM-based WF-integrated MMC-HVDC is worth exploring.

#### REFERENCES

- [1] J. Fang, F. Blaabjerg, S. Liu *et al.*, "A review of multilevel converters with parallel connectivity," *IEEE Transactions on Power Electronics*, vol. 36, no. 11, pp. 12468-12489, Nov. 2021.
- [2] R. Rosso, X. Wang, M. Liserre *et al.*, "Grid-forming converters: control approaches, grid-synchronization, and future trends-a review," *IEEE Open Journal of Industry Applications*, vol. 2, pp. 93-109, Apr. 2021.
- [3] J. Xi, H. Geng, and X. Zou, "Decoupling scheme for virtual synchronous generator controlled wind farms participating in inertial response," *Journal of Modern Power Systems and Clean Energy*, vol. 9, no. 2, pp. 347-355, Mar. 2021.
- [4] National Grid ESO. (2019, Aug.). Technical report on the events of 9 August 2019. [Online]. Available: <https://www.nationalgrideso.com>
- [5] L. Harnefors, M. Hinkkanen, U. Riaz *et al.*, "Robust analytic design of power-synchronization control," *IEEE Transactions on Industrial Electronics*, vol. 66, no. 8, pp. 5810-5819, Aug. 2019.
- [6] M. Li, Y. Wang, W. Hu *et al.*, "Unified modeling and analysis of dynamic power coupling for grid-forming converters," *IEEE Transactions on Power Electronics*, vol. 37, no. 2, pp. 2321-2337, Feb. 2022.
- [7] A. Tayyebi, D. Grob, A. Anta *et al.*, "Frequency stability of synchronous machines and grid-forming power converters," *IEEE Journal of Emerging and Selected Topics in Power Electronics*, vol. 8, no. 2, pp. 1004-1018, Jun. 2020.
- [8] C. Arghir and F. Dörfler, "The electronic realization of synchronous machines: model matching, angle tracking, and energy shaping techniques," *IEEE Transactions on Power Electronics*, vol. 35, no. 4, pp. 4398-4410, Apr. 2020.
- [9] M. Lu, "Virtual oscillator grid-forming inverters: state of the art, modeling, and stability," *IEEE Transactions on Power Electronics*, vol. 37, no. 10, pp. 11579-11591, Oct. 2022.
- [10] L. Harnefors, F. M. M. Rahman, M. Hinkkanen *et al.*, "Reference-feedforward power-synchronization control," *IEEE Transactions on Power Electronics*, vol. 35, no. 9, pp. 8878-8881, Sept. 2020.
- [11] L. Huang, H. Xin, and Z. Wang, "Damping low-frequency oscillations through VSC-HVDC stations operated as virtual synchronous machines," *IEEE Transactions on Power Electronics*, vol. 34, no. 6, pp. 5803-5818, Jun. 2019.
- [12] J. Guo, Y. Chen, S. Liao *et al.*, "Low-frequency oscillation analysis of VSM-based VSC-HVDC systems based on the five-dimensional impedance stability criterion," *IEEE Transactions on Industrial Electronics*, vol. 69, no. 4, pp. 3752-3763, Apr. 2022.
- [13] M. Li, P. Yu, W. Hu *et al.*, "Phase feedforward damping control method for virtual synchronous generators," *IEEE Transactions on Power Electronics*, vol. 37, no. 8, pp. 9790-9806, Aug. 2022.
- [14] L. Huang, H. Xin, H. Yuan *et al.*, "Damping effect of virtual synchronous machines provided by a dynamical virtual impedance," *IEEE Transactions on Energy Conversion*, vol. 36, no. 1, pp. 570-573, Mar. 2021.
- [15] L. Huang, H. Xin, H. Yang *et al.*, "Interconnecting very weak AC systems by multiterminal VSC-HVDC links with a unified virtual synchronous control," *IEEE Journal of Emerging and Selected Topics in Power Electronics*, vol. 6, no. 3, pp. 1041-1053, Sept. 2018.
- [16] R. Rosso, S. Engelken, and M. Liserre, "Robust stability analysis of synchronverters operating in parallel," *IEEE Transactions on Power Electronics*, vol. 34, no. 11, pp. 11309-11319, Nov. 2019.
- [17] Y. Liu, Y. Wang, M. Wang *et al.*, "Coordinated VSG control of photovoltaic/battery system for maximum power output and grid supporting," *IEEE Journal of Emerging and Selected Topics in Circuits and Systems*, vol. 12, no. 1, pp. 301-309, Mar. 2022.
- [18] X. Quan, R. Yu, X. Zhao *et al.*, "Photovoltaic synchronous generator: architecture and control strategy for a grid-forming PV energy system," *IEEE Journal of Emerging and Selected Topics in Power Electronics*, vol. 8, no. 2, pp. 936-948, Jun. 2020.
- [19] B. Pawar, E. I. Batzelis, S. Chakrabarti *et al.*, "Grid-forming control for solar PV systems with power reserves," *IEEE Transactions on Sustainable Energy*, vol. 12, no. 4, pp. 1947-1959, Oct. 2021.
- [20] Y. Ma, W. Cao, L. Yang *et al.*, "Virtual synchronous generator control of full converter wind turbines with short-term energy storage," *IEEE Transactions on Industrial Electronics*, vol. 64, no. 11, pp. 8821-8831, Nov. 2017.
- [21] F. Zhao, X. Wang, Z. Zhou *et al.*, "Control interaction modeling and analysis of grid-forming battery energy storage system for offshore wind power plant," *IEEE Transactions on Power Systems*, vol. 37, no. 1, pp. 497-507, Jan. 2022.
- [22] M. M. Kabsha and Z. H. Rather, "A new control scheme for fast frequency support from HVDC connected offshore wind farm in low-inertia system," *IEEE Transactions on Sustainable Energy*, vol. 11, no. 3, pp. 1829-1837, Jul. 2020.
- [23] M. Mehrabankhormartash, M. Saeedifard, and A. Yazdani, "Adjustable wind farm frequency support through multi-terminal HVDC grids," *IEEE Transactions on Sustainable Energy*, vol. 12, no. 2, pp. 1461-1472, Apr. 2021.
- [24] Y. Xiong, W. Yao, Y. Yao *et al.*, "Distributed cooperative control of offshore wind farms integrated via MTDC system for fast frequency support," *IEEE Transactions on Industrial Electronics*, doi: 10.1109/TIE.2022.3183355
- [25] Y. Xiong, W. Yao, Z. Shi *et al.*, "Adaptive dual droop control of MT-DC integrated offshore wind farms for fast frequency support," *IEEE Transactions on Power Systems*, doi:10.1109/TPWRS.2022.3179504
- [26] J. Lyu, X. Zhang, X. Cai *et al.*, "Harmonic state-space based small-signal impedance modeling of a modular multilevel converter with consideration of internal harmonic dynamics," *IEEE Transactions on Power Electronics*, vol. 34, no. 3, pp. 2134-2148, Mar. 2019.
- [27] K. Ji, S. Liu, H. Pang *et al.*, "Generalized impedance analysis and new sight at damping controls for wind farm connected MMC-HVDC," *IEEE Journal of Emerging and Selected Topics in Power Electronics*, vol. 9, no. 6, pp. 7278-7295, Dec. 2021.
- [28] M. Amin, A. Rygg, and M. Molinas, "Self-synchronization of wind farm in an MMC-based HVDC system: a stability investigation," *IEEE Transactions on Energy Conversion*, vol. 32, no. 2, pp. 458-470, Jun. 2017.
- [29] R. Yang, G. Shi, X. Cai *et al.*, "Autonomous synchronizing and frequency response control of multi-terminal DC systems with wind farm integration," *IEEE Transactions on Sustainable Energy*, vol. 11, no. 4, pp. 2504-2514, Oct. 2020.
- [30] C. Zhang, X. Cai, M. Molinas *et al.*, "On the impedance modeling and equivalence of AC/DC-side stability analysis of a grid-tied type-IV wind turbine system," *IEEE Transactions on Energy Conversion*, vol. 34, no. 2, pp. 1000-1009, Jun. 2019.
- [31] R. Pan, G. Tang, S. Liu *et al.*, "Impedance analysis of grid forming control based modular multilevel converters," *Journal of Modern Power Systems and Clean Energy*, vol. 11, no. 3, pp. 967-979, May 2023.
- [32] J. Sun and H. Liu, "Sequence impedance modeling of modular multilevel converters," *IEEE Journal of Emerging and Selected Topics in Power Electronics*, vol. 5, no. 4, pp. 1427-1443, Dec. 2017.
- [33] K. Ji, H. Pang, Y. Li *et al.*, "A hierarchical small-signal controller stability analysis method for the MMCs," *IEEE Transactions on Power Delivery*, doi: 10.1109/TPWRD.2021.3112382
- [34] J. Guo, Y. Chen, L. Wang *et al.*, "Impedance analysis and stabilization of virtual synchronous generators with different DC-link voltage con-

trollers under weak grid,” *IEEE Transactions on Power Electronics*, vol. 36, no. 10, pp. 11397-11408, Oct. 2021.

- [35] S. Zhu, K. Liu, X. Liao *et al.*, “*D-q* frame impedance modeling of modular multilevel converter and its application in high-frequency resonance analysis,” *IEEE Transactions on Power Delivery*, vol. 36, no. 3, pp. 1517-1530, Jun. 2021.
- [36] C. Yang, L. Huang, H. Xin *et al.*, “Placing grid-forming converters to enhance small signal stability of PLL-integrated power systems,” *IEEE Transactions on Power Systems*, vol. 36, no. 4, pp. 3563-3573, Jul. 2021.

**Rongcai Pan** received the B. Eng. and M. Sc. degrees in electrical engineering from Donghua University, Shanghai, China, in 2017 and 2020, respectively. He is currently pursuing the Ph.D. degree with the China Electric Power Research Institute, Beijing, China, and State Grid Smart Grid Research Institute, Beijing, China. His research interests include modeling and control of power systems with high penetration of renewables.

**Dong Liu** received the B.Sc. and M.Sc. degrees in electrical engineering from the Nanjing University of Science and Technology, Nanjing, China, in 2003 and 2007, respectively, and the Ph.D. degree from the China Electric Power Research Institute, Beijing, China, in 2012. From 2018 to 2019, he was a Post-Doctoral with Aalborg University, Aalborg, Denmark. His current research interests include power electronic control stability and interaction in voltage source converter (VSC) and modular multilevel converter (MMC) based DC transmission system, and physical and digital simulation technology.

**Shan Liu** received the B.S. degree in electrical engineering from Xi’an Jiao Tong University, Xi’an, China, in 2011, and the Ph.D. degree in electrical engineering from Tsinghua University, Beijing, China, in 2018. In 2018, he joined the State Grid Smart Grid Research Institute, Beijing, China, and

mainly focused on the system design and analysis of hybrid high-voltage direct current (HVDC) system. His research interests include DC bushing, transformer insulation, and HVDC systems.

**Jie Yang** received the B.Eng. and Ph.D. degrees in electrical engineering from Tsinghua University, Beijing, China, in 2005 and 2011, respectively. In 2011, he joined the China Electric Power Research Institute (CEPRI), Beijing, China, and mainly focused on the system design and analysis of voltage source converter based high-voltage direct current (VSC-HVDC) system. In 2012, he joined the Global Energy Interconnection Research Institute (GEIRI), Beijing, China. His research interests include the control and protection strategies of VSC and novel HVDC converter technologies.

**Longze Kou** received the B.S. degree in electrical engineering from the China University of Mining and Technology, Xuzhou, China, in 2010, and the M.S. degree in electrical engineering from the University of Duisburg-Essen, Duisburg, Germany, in 2014. In 2014, he joined Global Energy Interconnection Research Institute Company, Ltd., (GEIRI), Beijing, China. His current research interests include design and control of voltage source converter (VSC) and modular multilevel converter (MMC) based DC system, MMC digital and physical simulation technology, and MMC hardware-in-loop testing technology.

**Guangfu Tang** received the B. S. degree in electrical engineering from Xi’an Jiao Tong University, Xi’an, China, in 1990, and the M.S. and Ph.D. degrees in electrical engineering from the Institute of Plasma Physics, the Chinese Academy of Sciences (ASIPP), Hefei, China, in 1993 and 1996, respectively. Now, he is an Academician of the Chinese Academy of Engineering and President of State Grid Smart Grid Research Institute (SGRI), Beijing, China. His current research interests include high-power electronics technology for reliable operation of large interconnected power grids, relocatable DC device system, and voltage source converter based high-voltage direct current (VSC-HVDC) transmission.